

1 Replay as structural inference in the hippocampal-entorhinal 2 system

3 Talfan Evans^{123,#} and Neil Burgess^{12,#}

4 1 Institute of Cognitive Neuroscience, UCL

5 2 Institute of Neurology, UCL

6 3 CoMPLEX, UCL

7 #correspondence

8 **Abstract**

9 Model-based decision making relies on the construction of an accurate representation of the
10 underlying state-space, and localization of one's current state within it. One way to localize is to
11 recognize the state with which incoming sensory observations have been previously associated.
12 Another is to update a previous state estimate given a known transition. In practice, both strategies are
13 subject to uncertainty and must be balanced with respect to their relative confidences; robust learning
14 requires aligning the predictions of both models over historic observations. Here, we propose a dual-
15 systems account of the hippocampal-entorhinal system, where sensory prediction errors between these
16 models during *online* exploration of state space initiate *offline* probabilistic inference. *Offline*
17 inference computes a *metric* embedding on grid cells of an *associative* place graph encoded in the
18 recurrent connections between place cells, achieved by message passing between cells representing
19 non-local states. We provide testable explanations for coordinated place and grid cell 'replay' as
20 efficient message passing, and for distortions, partial rescaling and direction-dependent offsets in grid
21 patterns as the confidence weighted balancing of model priors, and distortions to grid patterns as
22 reflecting inhomogeneous sensory inputs across states.

23 Author Summary

- 24 • Minimising prediction errors between transition and sensory input (observation) models
25 predicts partial rescaling and direction-dependent offsets in grid cell firing patterns.
26 • Inhomogeneous sensory inputs predict distortions of grid firing patterns during *online*
27 localisation, and local changes of grid scale during *offline* inference.
28 • Principled information propagation during *offline* inference predicts coordinated place and
29 grid cell ‘replay’, where sequences propagate between structurally related features.

30 Introduction

31 Grid cells in the medial entorhinal cortex (mEC), whose firing fields form a periodic hexagonal lattice
32 across the environment, are thought to support path integration^{1–3}, whereas hippocampal place cells
33 tend to have unimodal firing fields reflecting environmental cues such as boundaries^{4,5}. Grid cell
34 firing patterns are stable over time, suggesting corrective environmental inputs, possibly from place
35 cells⁶, but rely more on self-motion than place cell firing patterns⁷ suggesting that environmental
36 inputs are not fully corrective^{2,8,9}. Given estimates of each input’s uncertainty, Bayesian inference tells
37 us how they should be optimally combined.

38 Although *online* learning (i.e. using only currently available sensory information) can converge under
39 low PI and sensory noise, robust learning in the presence of noise requires minimizing the error
40 between self-motion and environmental estimates of location across all state transitions^{10,11}. Thus,
41 historic observations must be stored and revisited *offline* (i.e. independently of current sensory inputs)
42 to allow propagation of local environmental information to non-local but structurally connected
43 regions of the cognitive map, e.g. as when adapting to a novel shortcut or barrier. This process can
44 also be viewed as an embedding of sensory experience within a low-dimensional manifold (in this
45 case, 2D space), as observed of place cells during sleep¹².

46 Building on previous work^{11,13–15}, we propose a dual-systems (*online-offline*) account of spatial
47 inference in the hippocampal/entorhinal system, which we define as the process of identifying the

48 configuration of both one's own location (current state) and the location of environmental landmarks
49 in space (c.f. 'SLAM'¹⁰). In familiar environments, *online* localization (identification of one's own
50 position) is achieved by recursively combining self-motion and sensory inputs, which are mediated by
51 learned *transition* and *observation* models, respectively. However, prediction errors between these
52 models trigger *offline* inference over non-local states, facilitating fast learning of new or changed
53 associative environmental structure, encoded *online* in place-place cell synaptic associations. We
54 identify this *offline* inference with coordinated hippocampal/mEC 'replay'^{16–20}.

55 Our framework also provides algorithmic- and implementation-level explanations for observed
56 features of grid cell firing in response to manipulations^{7,9,21–24} or inhomogeneity^{25–29} of environmental
57 sensory input. Overall, these phenomena can be understood in a probabilistic framework, where
58 minimization of prediction errors between the transition and observation models are traded against
59 prior model beliefs.

60 Results

61 Probabilistic *online* localization with place and grid cells

62 Grid cells exist in 'modules' of cells, whose firing patterns have the same spatial scale and orientation
63 relative to the environment, but differ in their spatial offsets³⁰. The spatial scale increases in discrete
64 steps along the dorso-ventral axis, suggesting that, across modules, GCs support a hierarchical
65 representation of space^{21,24,31–33}. Here, we consider a single module of GCs, whose activity represent a
66 probability distribution over a periodic, discretized region of space (visualised as a topographically
67 arranged sheet of cells; Fig. 1A).

68 The self-location distribution is maintained over time by recursively integrating sensory and self-
69 motion inputs, accounting for their uncertainties (Fig. 1A). Firstly, the posterior distribution over
70 agent location (grid module activity) from the previous time-step \mathbf{G} is updated given noisy perceived
71 movement $\hat{\mathbf{u}}$ via the *transition model* T (see Methods):

$$72 \quad G'(\mathbf{x}) = \int T(\mathbf{x}, \mathbf{x}' | \hat{\mathbf{u}}, \boldsymbol{\alpha}) \cdot G(\mathbf{x}') d\mathbf{x}' \quad (1)$$

73 where \mathbf{x} is the 2D coordinate of the agent location in *metric* space (corresponding to a particular grid
74 cell) and \mathbf{x}' the location at the previous time-step. Biophysically, T would be represented by a
75 population of direction dependent ‘shifter’ cells with asymmetric recurrent weights¹ with a circulant
76 structure³⁴ (Fig. S1C, see Methods) learned *a priori* (but see Refs. ^{35–37}). The rate of translation of
77 activity on the grid sheet in response to movement $\hat{\mathbf{u}}$ is controlled by the *transition model* gain $\boldsymbol{\alpha} =$
78 $[\alpha_x, 0; 0, \alpha_y]$, which might correspond to the strength of the associations to, or the speed dependence
79 of, shifter or conjunctive cells^{31,38,39} (see Supplementary Methods).

80 The *transition model* estimate $G'(\mathbf{x})$ is then refined by observations of environmental features, which
81 map to *metric* space locations via *observation model* H :

$$82 \quad G(\mathbf{x}) = \frac{1}{K} H(\mathbf{P}|\mathbf{x}) \cdot G'(\mathbf{x}) \quad (2)$$

83 where \mathbf{P} is a vector of place cell firing rates, firing of place cell i representing the likelihood of the
84 presence of a specific sensory feature, or combination thereof. In our simulations, these have unique
85 locations in physical space $\boldsymbol{\mu}_i$ and receptive field widths Σ_{PC}^i . Where the number of grid cells is large,
86 the weights from place cell i to the grid module define a distribution for that feature’s estimated
87 location in *metric* space (Fig. 1A). The weighted projection of place cell activity by these weights
88 defines the *observation model* H . K provides inhibitory normalization (see Supplementary Methods).

89 *Online* learning modifies the *observation model* to reflect the current *transition model* location
90 estimate (induces synaptic changes in the place-grid cell connection weights via a BCM rule; Fig. 2A;
91 Methods). *Online* learning produces stable grid patterns (due to the circulant structure of T) for a
92 range of levels of PI and sensory noise, but convergence fails in higher noise regimes (Fig. S2B).
93 After a short period of initial learning, stable grid patterns emerge in the integrated estimate, despite
94 the pure PI estimate being too noisy and the sensory associations too immature to drive stable
95 patterns, if operating independently (Fig. 1B).

96 *Offline inference: The hippocampus as a probabilistic graph*

97 Local, *online* learning is not robust in novel environments, because corrections to the estimated agent
98 location (current grid cell activity), e.g. upon encountering familiar environmental features (place cell
99 activity) associated to a different location on the grid module, also imply corrections to the encoding
100 of feature observations along the preceding trajectory¹⁰. That is to say; local updates to the *cognitive*
101 *map* also imply non-local, structurally associated changes. Formally, probabilistic spatial inference in
102 this case requires finding the most likely configuration of *metric* space feature locations
103 $\{\mathbf{b}_i\}_{i=1:N_P}$ (each \mathbf{b}_i is the 2D coordinate of feature i in *metric* space, i.e. a place - grid cell association)
104 and agent location \mathbf{x} (the distribution over which is indicated by the grid cell firing rates) consistent
105 with environmental sensory observations made along a given trajectory.

106 Theoretically, the configuration $\{\mathbf{b}_i\}_{i=1:N_P}$ can be recovered purely from the distances between pairs
107 of environmental features¹⁰ (Fig. 1F, “square”, “ring”). Importantly, despite both feature locations
108 being susceptible to large absolute errors (due to noisy PI), the errors will be correlated such that
109 pairwise distance measurements will decrease in variance with observations¹⁰. This method predicts
110 characteristic failure modes when the pairwise distance information is ambiguous or incomplete (e.g.,
111 Fig. 1F; “broken ring”). New distance observations might also cause dramatic changes to the inferred
112 configuration (e.g. the discovery of a shortcut). If the current *absolute* estimates of feature node (i.e.
113 place cell) location are stored in the place-grid cell synaptic weights, we propose that the *relative*
114 *distances* between pairs of features are stored in the recurrent weights between place cells in
115 hippocampal region CA3.

116 Consider a spring network, where the edge between environmental feature nodes i and j represents a
117 noisy pairwise observation with length reflecting pairwise distance and stiffness reflecting
118 certainty^{13,40} (Fig. 1F, S6A). Minimizing the elastic energy in the spring mesh system corresponds to
119 finding the maximum of the joint likelihood $L(\cdot)$, which is a function of the feature locations in *metric*
120 space $\{\mathbf{b}_i\}_{i=1:N_P}$ and the internal gain parameter α , given pairwise distance measurements with

121 Gaussian noise (δ_{ij}). This is equivalent to defining a probabilistic graphical model (see Methods) over
122 the posterior:

123
$$L(\mathbf{b}_1, \dots, \mathbf{b}_{N_p}, \boldsymbol{\alpha}) \propto p(\boldsymbol{\alpha}|\boldsymbol{\alpha}_0) \prod_{(i,j) \in E} \psi(\mathbf{b}_i - \mathbf{b}_j, \boldsymbol{\alpha}|\delta_{ij}) \prod_{i=1:N_p} B_i(\mathbf{b}_i) \quad (3)$$

124 where the current PC-GC weights B (B_i is the probability distribution of the location of feature i and
125 $B_i(\mathbf{b}_i)$ is its value at *metric*/grid module location \mathbf{b}_i) act as priors on the feature node locations, the
126 pairwise potential terms $\psi(\cdot)$ penalize the difference between *associative* pairwise distance
127 measurements δ_{ij} made directly in environmental *stimulus* space, and the distance between their
128 candidate locations in *metric* space $\mathbf{b}_i - \mathbf{b}_j$. E is the set of connected PCs (see Methods). Distance in
129 *metric* space is also a function of the *transition model* gain ($\boldsymbol{\alpha}$), which has a Gaussian prior $p(\boldsymbol{\alpha}|\boldsymbol{\alpha}_0)$
130 (a larger $|\boldsymbol{\alpha}|$ will decrease the *metric* space distance for all pairs; see Methods). Maximizing the
131 likelihood (finding the state of minimum energy in the spring network) model over all feature node
132 pairs minimizes the total prediction error between *associative* and *metric* generative models of the
133 world¹⁵ (Fig. S7).

134 The *associative* distances can be straightforwardly learned during *online* exploration. Since Hebbian
135 learning reflects coactivity, a trajectory exploring the environment uniformly results in synaptic
136 strengths between place cells proportional to the spatial correlation between their receptive fields⁴¹. The
137 Euclidean separation between their fields is then accessed via a simple transformation (see Methods;
138 Fig. S1G). In this context, learning the PC-GC weights (modifying the *observation* model) during *online*
139 localization corresponds to forming spatial priors over feature locations which anchor the structure,
140 which would otherwise be translation or rotation invariant (since measurements are relative), learned
141 during *offline* inference to constant locations on the grid-map. Taken together, our framework proposes
142 a mapping onto anatomy of the joint *agent-feature* location distribution required for full probabilistic
143 inference over environmental structure (Fig. S5; See overall algorithm in Table S1).

144 **Partial grid pattern responses to environmental rescaling**

145 Uniform rescaling of an environment will introduce a mismatch between the estimates of location
146 from the *transition* and *observation* models (i.e. a ‘prediction error’). To minimize these prediction
147 errors, the *offline* system can either modify the *transition* model gain to match the current
148 environmental input (Fig. 2A, bottom), or modify the mapping from environmental inputs to *metric*
149 space in the *observation* model (Fig. 2A, middle; see Methods). The degree to which either is
150 modified should reflect their relative confidences, specified by a ‘transition confidence score’ ($T_C =$
151 $\sigma_{obs}^2/\sigma_\alpha^2$, the ratio of confidence in the *transition* vs *observation* models; see Methods). Similarly, a
152 ‘prior confidence score’ P_C specifies how much the system will tolerate persistent prediction errors; if
153 P_C is large, optimization may favour preserving prior configurations, as opposed to alignment of the
154 current *transition* and *observation* models (see Methods).

155 We modelled experiments in which the physical environment^{21,42} and perceived velocity through a
156 visual virtual environment⁷ were re-scaled, such that self-motion and sensory inputs conflicted. In
157 both experiments, the rescaling of the grid patterns was *partial*, i.e. less than the magnitude of the
158 physical or virtual manipulation, and less than those of place fields.

159 Both manipulations can be simulated by introducing a visual gain parameter α^{Visual} to the simulation
160 of the environment (in both experiments it scales the amount of self-motion required to traverse the
161 width of the perceived environment). Learned *associative* distances (δ) are also scaled by this
162 parameter, reflecting its effect on the temporal overlap of place fields (see Methods Eq. 12). We
163 simulated grid pattern rescaling responses over a range of transition confidence scores T_C . When
164 confidence in the *transition* model is high ($T_C \rightarrow \infty$), grid patterns in the real world are unchanged
165 when plotted against physical movement (but are changed when plotted in visual VR coordinates; Fig.
166 2B, first column). The opposite is true when confidence in the *observation* model is high: grid
167 patterns are unchanged relative to the apparent environment (Fig. 2B, last column).

168 However, for intermediate T_C values (i.e. balanced confidence in the *transition* and *observation*
169 models), the model predicts partial rescaling of the grid pattern relative to the size of the manipulation

170 (Fig. 2B, middle column), matching the observed grid patterns in both experiments^{7,21} (and a similar
171 third experiment in on a virtual linear track⁴³; Fig. 2C).

172 Differential grid and place field responses to environmental reshaping

173 How does the *offline* system respond to more complex environmental deformations? When one wall
174 of a familiar rectangular environment is rotated inwards by 45°²², place fields near the wall shifted
175 almost fully while fields further away remained largely stationary, consistent with place fields
176 preferentially reflecting local environmental inputs⁵. In contrast, grid fields shifted only partially near
177 to the manipulated wall. Using the observed place field shifts²³, we simulated the response of grid
178 cells to the same manipulation (Fig. 3; see Supplementary Methods). Shifted place fields induce a
179 misalignment between the *associative* distances and the distance between their encodings in *metric*
180 space. The place field shifts are local and non-uniform, and so misalignment cannot be corrected by a
181 global change to the *transition gain* α . Indeed, α is not significantly modified during the optimization
182 process, regardless of the T_C value. Instead, alignment between the *transition* and *observation* models
183 is maximized by modifying the *observation model*, i.e. updating the locations of the place fields on
184 the grid module.

185 If there were no confidence in the prior *observation* model ($P_C \rightarrow 0$), it would be modified offline to
186 match the transition model, leaving the grid pattern unperturbed by the environmental change (Fig.
187 3B,C, top row). At the other extreme, favouring prior beliefs over recent observations (i.e. pairwise
188 distances encoded during the manipulation trial) would result in an unchanged *observation* model, and
189 grid field shifts that exactly mirror corresponding place field shifts (Fig. 3B,C, bottom row). In this
190 regime, there would be permanent misalignment of the *transition* and *observation* models during
191 *online* localization, producing noisy grid patterns, as when simulating a related experiment where grid
192 distortions were observed in trapezoid environments⁴⁴ (Fig. S2D). Setting P_C to an intermediate value
193 reproduces the experimentally observed partial shifting of grid fields (relative to the place fields²³)
194 when visualizing the structure encoded in the *observation* model (i.e. assuming low confidence in the
195 transition model; Fig. 3B,C and D).

196 **Direction dependent shifting of grid patterns during *online* localization**

197 In addition to partial changes to grid scale in response to environmental rescaling, enduring
198 misalignments between *observation* and *transition* models can result from strong model priors, which
199 prevent complete adaptation of the *transition* model gain. These cause the *transition* estimate to
200 consistently precede that of the *observation* model, in the current direction of travel (on a 1D track,
201 Fig. 2E) during VR visual gain decrease trials or physical expansion of the environment.

202 In all three cases, the integrated estimate of location (Eq. 2) in the *online* model converges to a fixed
203 distance ahead of the *observation* model estimate (in the direction of travel; Fig. 2E inset and 3D),
204 causing the grid pattern in the real world to dynamically shift opposite the direction of travel, as
205 observed experimentally^{7,9}. Our model suggests that the offsets should be partial (smaller than implied
206 by a hard-reset at the boundary) and not specifically require a recent boundary encounter (cf. Keinath
207 et al.⁹). Dynamic shifting in the model will reduce with experience of the novel or manipulated
208 environment, as model misalignment reduces, as observed experimentally⁴⁵.

209 ***Online* and *offline* perceptual warping in spatial representations**

210 With increasing experience of an environment, grid firing patterns exhibit both local scale changes²⁶
211 and global shear-like distortions²⁹, the latter associated with 7.5-8° offsets of one of the grid axes^{29,44}
212 to the walls of square environments. Both effects were present in our simulations and can be attributed
213 distinctly to the *offline* map-learning and *online* localization components of our theoretical
214 framework.

215 Firstly, we show that local changes to the grid scale²⁶, which are positively correlated with
216 behavioural occupancy (animals spend more time in the middle of the environment), arise from the
217 *offline* process of map (PC-GC connections) learning. These mapping-induced distortions can be
218 further subdivided into two mechanisms, both of which induce local scale changes by biasing the
219 pairwise distances recovered from the Hebbian learned recurrent connections in CA3 (Fig. 1D,4; Fig.
220 S7).

221 Firstly, relative behavioural under-sampling of the place fields near the boundaries of the environment
222 (using occupancy statistics from²⁶; Fig. 4A, bottom) lead to weaker PC-PC connections, and
223 consequent overestimation of their pairwise distances, producing local scale changes (Fig. S7C).

224 Secondly, since Hebbian learned connection weights between place cells reflect the correlation in
225 their firing, and therefore their statistical discriminability⁴⁶, two place cells with broad receptive fields
226 would develop a stronger connection than a pair with equal separation but narrower receptive fields
227 (stronger connections correspond to shorter distances on the grid module, producing grid patterns with
228 larger scales in the environment; Fig. 1D). Another recent study⁴⁷ suggests that place fields are
229 narrower near the edges of an environment, consistent with greater precision when driven by more
230 proximal environmental features⁵ (Fig. 4A, top row). In our model, this produces weaker recurrent
231 connections and a shrinking of the grid pattern at the edges of the environment following *offline*
232 inference (Fig. 4D,E, top row).

233 Together, our results suggest that the cognitive ‘distance’ between two sensory features should be
234 greater both when the absolute confidence in their spatial locations is greater (reflecting an increased
235 statistical discriminability), or when those features are under-sampled relative to other features.

236 Although the action of both mechanisms are independent their effect is the same; both i) relative
237 under-sampling of the transition between two adjacent states and ii) a reduced statistical
238 discriminability between those states, both contribute to a weaker pairing of their representative place
239 cells, resulting in greater separation between their encodings in *metric* space and a locally larger grid
240 scale when ‘read-out’ in the firing pattern (a locally larger perception of distance).

241 In contrast, global shear-like distortions²⁹ and associated 7.5-8° offsets of one of the grid axes^{29,44} can
242 be interpreted as *localization* induced distortions during *online* exploration. In Stensola et al.²⁹, rats
243 were introduced into the same corner of the box at the start of each trial; in Butler et al.²⁵, shearing
244 developed following the introduction of reward²⁵. In both experiments, shearing developed with
245 increasing experience^{25,29}. We hypothesized that these distortions reflect an increasing effect of non-

246 uniform environmental inputs to the grid module, either reflecting their natural distribution^{25,29} or
247 inhomogeneous behavioural sampling of environmental locations²⁶.

248 In our simulations, given a learned map, biasing the strength of sensory inputs at specific locations
249 (e.g. one/two corners) during *online* exploration reproduced several experimentally characterized
250 global distortions by causing a bias in the decoding of location (i.e. salient locations contribute a
251 larger ‘vote’; Fig. S3; see Supplementary Methods).

252 Probabilistic inference through HPC-mEC message passing

253 To this point we discussed, from a functional perspective, how the brain might optimize its internal
254 representations to reflect the uncertainty of sensory information. But how might the brain perform this
255 optimization? In the above analyses of *offline* inference, we numerically computed the maximally
256 likely feature locations on the grid module. However, the system must also track the uncertainty in
257 these estimates, which would require updating the place-grid cell weights (including those with firing
258 fields far from the agent location). An update of the full weight distributions is generally intractable
259 when the state space is large.

260 Belief propagation⁴⁸ is a technique for approximating this inference on graph structured data, and
261 comprises two stages. First, a given feature node (i.e. a place cell) computes its location distribution
262 (i.e. connections to the grid cells) $B_i(\mathbf{b}_i)$ by multiplying its prior $B_i^{(0)}(\mathbf{b}_i)$ with messages received
263 from its connected neighbours (Fig. 5C; see Methods for details). A message $m_{i \rightarrow j}(\mathbf{b}_j)$ expresses
264 neighbour node i ’s belief of node j ’s location, conditioned on its own distribution, and is dependent
265 on the same pairwise potential terms $\psi(\cdot)$ in Eq. 3. The effect of a message is to favour distributions
266 of nodes i and j which locate them at a radial distance equal to the associative distance δ_{ij} ; causing
267 messages to be expressed as rings centred on the belief of the broadcasting node (Fig. 5C). Resolving
268 a feature’s unique location then depends on aggregating messages from multiple neighbours (Fig. 5C).
269 Computations are distributed, and importantly only require information that is local to each neuron.

270 Each node in the graph iterates between updating its belief and broadcasting messages, converging
271 when new messages cease to change the beliefs of their recipient nodes. As expected, the reduction in

272 pairwise prediction error between associative distances and their corresponding distances in grid
273 space (see Methods) over successive message iterations is accompanied by a sharpening of the
274 distribution of each feature's location on the grid module (see Supplementary Methods; Fig. S1H).

275 *Offline inference triggered by prediction errors*

276 How might the *online* and *offline* systems interact? If the *online* system is sufficient to localize within
277 pre-learned, simple or slowly changing environments, non-local reactivations of place cells would be
278 unnecessary. However, more complex *offline* inference is required under more demanding
279 circumstances, or in novel or changing environments. We hypothesize that *offline* or ‘remote’
280 inference is triggered by *prediction errors* between location estimates from the *transition* and
281 *observation* models, respectively (Fig. 1G), defined in our model as the Kullback-Leibler divergence
282 $\epsilon = \text{KL}(G', H)$.

283 Prediction errors are large when the *observation model* prediction (weighted place cell input) is
284 different and more sharply peaked than the *transition model* estimate (Fig. 1G; see Methods;
285 prediction errors will not be generated in absence of incoming sensory information, as in darkness,
286 when the observation model estimate is uncertain).

287 To illustrate our *dual-systems* (*online+offline*) hypothesis (Fig. S7), we simulated an agent navigating
288 around a novel circular track (the *loop closure* task; Fig. 5). Completion of the first lap produces
289 positive prediction errors between the sharply peaked input from feature inputs learned at the
290 beginning of the trial, and the agent location estimate which is uncertain given the accumulation of PI
291 noise (Fig. 5B).

292 Decrease in structural error (the difference between the place field separations and their encoded
293 separations on the grid cell sheet) following *online+offline* inference was markedly larger than
294 following *online* learning alone (Fig. 5E). The inferential power of this ‘one-shot’ learning process
295 derives from consideration of the full covariance structure of the feature locations (captured by the
296 CA3 connection weights between place cells), compared to the purely local learning occurring *online*.

297 The system was subsequently able to navigate with dramatically reduced error (Fig. 5Aiv),
298 eliminating prediction errors on subsequent lap completions (Fig. 5B; Supplementary Video 1).

299 **Coordinated grid-place cell replay as structured information propagation**

300 The *scheduling* of updates in belief propagation is important because messages that do not change the
301 beliefs of neighbours are redundant (Fig. 6A). We scheduled only the place cell whose belief had
302 changed most to broadcast a new message on each cycle (Fig. 6A; see Methods). This *max-update*
303 scheduling was more efficient than simple synchronous schemes, converging with fewer messages
304 (Fig. 6C; see Ref.⁴⁹).

305 The sequences of place cells broadcasting messages during *offline* inference in the loop-closure
306 simulation have significant structure (6B). They tend to initially propagate backwards along the track
307 from the animal's current position, resembling the characteristic reverse hippocampal replay
308 following reward¹⁷ (Fig. 6B), but also occasionally hop to new locations where remote sequences are
309 initiated⁵⁰ (Fig. 6B,F). These subsequent sequences showed an approximately equal distribution of
310 forward/reverse sweeps (Fig. 6D; see Methods; Supplementary Video 1).

311 Thus, hippocampal ‘replay’ may reflect correction of local regions of the cognitive graph given new
312 or ‘surprising’ information, as opposed to simple recapitulation of experience⁵¹. Sequences selectively
313 affect place cells whose beliefs are structurally affected, and terminate when this is no longer the case,
314 ‘hopping’ to remote regions. This leads to smooth sequences in un-converged graphs (novel
315 environments) and more hoppy sequences with experience, where converged regions may be skipped
316 (Fig. 6F). These ‘hops’ marked the separation of ‘replay’ events into distinct sub-sequences (see
317 Methods). Multiple trajectories may also be played out in parallel (e.g. two trajectories alternating
318 under max-scheduling; Fig. 6B, middle, grey shading).

319 **A neural model of coordinated place cell – grid cell replay**

320 How might belief propagation for *offline* inference be implemented in spikes fired by place and grid
321 cells during replay? We propose a schematic model with a focus on function rather than biological
322 detail (e.g. our ‘place cells’ combine the recurrent connections of CA3 with the connections to mEC

323 of CA1). In the model, minimizing prediction errors between *associative* and *metric* generative
324 models corresponds to synchronizing the propagation of activity through CA3 and mEC, respectively
325 (Fig. 7; see Supplementary Methods; Supplementary Video 2). A ‘message’ is initiated by a place cell
326 spike, which propagates in CA3 via the Hebbian recurrent connections that encode place field
327 separations. In parallel, the same spike initiates activity at the corresponding location on the grid cell
328 module, which then propagates on the grid sheet as a traveling wave, using the same circuitry as path
329 integration in the *online* model and propagating at the same speed as spikes in CA3 (see Methods).
330 Hebbian-like learning strengthens connections from place cells to grid cell which simultaneously
331 receive input in CA3 and EC respectively (Fig. 7A), approximating the algorithmic message-passing
332 implementation (Fig. 7B, C). Firing of the broadcasting place cell is triggered by changes in its
333 synaptic weights to the grid cell population, reflecting correction of the observation model in response
334 to prediction error with the transition model (see Supplementary Methods).

335 Discussion

336 Building on previous work^{11,13,15}, we argue that the mEC-HPC system performs spatial inference in
337 two distinct regimes. Given a known ‘cognitive map’ (mapping sensory information to metric space),
338 probabilistic integration allows optimal estimation of current location by *online* combination of
339 uncertainty-weighted self-motion and environmental observations provided by *transition* and
340 *observation* models respectively (Fig. 1). Where these estimates deviate strongly, prediction errors
341 (Fig. 1G) trigger *offline* inference events (Fig. 5B), which propagate local environmental input to
342 remote but structurally associated states, producing coordinated (often sequential) reactivations in
343 place and grid cells (Fig. 6, 7). The effect of *offline* inference is to produce a 2D embedding of the
344 sensory information provided through the place cells, which may facilitate planning or generalization.
345 Although not modelled here, back-projections from grid to place cells, reflecting the metric
346 embedding of their place fields, might therefore also reduce uncertainty in place cells’ firing,
347 producing increased spatial stability in their fields, as observed to occur during sleep¹².

348 Partial rescaling of grid patterns^{7,21} and differential shifting of grid and place fields²³ in response to
349 manipulations of environment sensory input can be understood as joint optimization of *transition* and

350 *observation* models, balancing model priors with new observations. Where prediction errors persist,
351 direction dependent grid pattern shifts may emerge as a result of probabilistic integration of these
352 conflicting cues^{7,9} (whereas boundary-dependent resetting⁹ produces larger shifts than experimentally
353 observed and no rescaling; Fig. 2D, E).

354 We show that observed grid pattern distortions can be mechanistically linked to inhomogeneity in the
355 sampling or neural representation of the environment^{25,26,29} (Figs. 4A, S3), which might be reflected in
356 behaviour⁵². Thus variation in the confidence, sampling or discriminability of sensory states will
357 produce local changes in grid scale, inducing non-Euclidean structure in the *metric* representation of
358 space (Fig. 1D, 4B). Our model also shows that distortions appear gradually with experience²⁹, as the
359 learned mapping from sensory features to metric space (the *observation* model) becomes more
360 confident relative to the estimate of location from path integration (the *transition* model). Given initial
361 learning, *online* localization errors (Fig. S3) should occur immediately following subsequent
362 manipulations to the environmental sensory input, whereas *offline* changes may occur over longer
363 timescales and correlate with replay of the manipulated states (Figs. 4,6; consistent with grid, but not
364 place fields reorganizing significantly during sleep⁵³). However, although large prediction errors will
365 cause more easily detectable *offline* inference events, *offline* learning may occur continuously and not
366 necessarily reactivate distinct previously experienced spatial trajectories⁵¹. We note that strong
367 *associative* connectivity may also contribute to pattern completion, making the place cell
368 representation robust to cue removal⁵⁴.

369 Theoretical studies have demonstrated how the connectivity of the mEC *metric* space might emerge
370 from a low-dimensional embedding of sensory stimuli⁵⁵, predictive states³⁵ or from unsupervised
371 learning during navigational tasks⁵⁶. A crucial difference in our model is that perceptually similar but
372 physically separated compartments will be represented distinctly⁵⁷, reflecting the vectorial translation
373 between them in the transition model (i.e., not simply reflecting the topological state transition
374 structure³⁵). Another recent model showed that grid cell like responses can emerge from learning the
375 transition model that best predicts observed sensory stimuli³⁶. We instead assume a fixed transition
376 structure but with a variable linear gain, consistent with continuous attractor models³¹ where

377 translation of activity on the grid cell sheet is driven by cells with velocity-dependent firing rates^{38,39}.

378 Indeed, a recent study showed that velocity dependence in mEC firing is tied to environmental
379 manipulations³⁹.

380 We propose that *offline* structural inference events correspond to coordinated HPC/mEC replay^{16–19,58–}
381 ⁶⁰, which can be viewed as synchronizing predictions from *associative* (CA3) and *metric* (mEC)
382 generative models (Fig. S7). In this way, structural changes to an environment can be propagated to
383 non-local regions of the *metric* embedding, in contrast to models in which these states need to be
384 physically revisited¹³, consistent with the observation that replays do not necessarily repeat
385 experienced trajectories⁵¹. Prediction errors between the two models may trigger replay events and
386 corresponding sharp-wave ripples^{61,62}. To our knowledge, this is the first functional model of
387 coordinated place cell-grid cell replay¹⁸ (although cf. Ref. ⁶³), and provides an alternative to reward-
388 based theories^{64,65} (we note that rewards may themselves represent salient sensory features,
389 independent of their reward value).

390 Our model makes a number of experimentally testable predictions. Firstly, systematic manipulation of
391 the discriminability of sensory cues distributed within an environment should produce predictable
392 distortions to the grid pattern, observed with increasing experience of an environment. Secondly,
393 replay should be more frequent after structural changes such as shortcuts, blockages or gain
394 manipulations as in the experimental setup of Fig. 5. Thirdly, replay events triggered by specific
395 unexpected sensory observations should become less frequent (Fig. 5B) and smooth (Fig. 6E, F) with
396 continued experience, if the observations remain stable. Fourthly, multiple local replay events may
397 occur in inter-leaved fashion (Fig. 6C, *middle*, grey shading). Fifthly, we predict the existence of
398 travelling waves in grid cells (as a function of their spatial phase; see also^{66,67}, Fig. 7). Lastly, initial
399 messages propagating from the animal’s current location may not cause subsequent messages in
400 remote regions of the graph which are already sufficiently converged (messages will not cause
401 changes in the beliefs of their recipients), although activity in mEC will continue to propagate. Thus
402 grid cell replay could thus be detectable in the absence of simultaneous place cell replay¹⁹ (but place
403 cell replay requires the grid cell *transition* model and so depends on mEC⁶⁸).

404 Our proposed structure learning framework can account for diverse phenomena observed in the HPC-
405 mEC system, and makes several novel, experimentally testable predictions.

406 Methods

407 *Online recursive Bayesian estimation*

408 The transition matrix T defines the probability of transitioning from agent location \mathbf{x}' to location \mathbf{x} ,
409 and is a function of the perceived current velocity $\hat{\mathbf{u}}$ and *transition* model gain $\boldsymbol{\alpha} = [\alpha_x, 0; 0, \alpha_y]$.
410 Since our *metric* space is periodic, T accounts for cyclic transitions \mathbf{c}_{mn} , with Gaussian noise
411 proportional to the perceived velocity $\hat{\mathbf{u}} \sim \mathbf{u} + N(0, \text{diag}(\mathbf{u})\Sigma_{\text{PI}})$:

$$412 T(\mathbf{x}, \mathbf{x}' | \hat{\mathbf{u}}, \boldsymbol{\alpha}) = \sum_{mn=-\infty}^{\infty} f(\mathbf{x} - \mathbf{x}' | \hat{\mathbf{u}} + \mathbf{c}_{mn}, \text{diag}(\hat{\mathbf{u}})\boldsymbol{\alpha}^{-1}\Sigma_{\text{PI}}) \quad (7)$$

413 where $f(\mathbf{x} | \boldsymbol{\mu}, \boldsymbol{\Sigma})$ is a multivariate Gaussian PDF, $\mathbf{c}_{mn} = 2\boldsymbol{\alpha}^{-1}(m\mathbf{v}_1 + n\mathbf{v}_2)$ and $\mathbf{v}_1 =$
414 $[\cos(\phi), \sin(\phi)]$ and $\mathbf{v}_2 = [\cos\left(\phi + \frac{\pi}{3}\right), \sin\left(\phi + \frac{\pi}{3}\right)]$ define the unit vectors of a hexagonal lattice⁶⁹
415 with grid pattern orientation ϕ and $\text{diag}(\cdot)$ produces a diagonal matrix from a vector input. Since
416 most of the mass is associated with shorter transitions, in practice we approximate the full distribution
417 with a finite number of periodic summations (i.e. ignore the tails; 5 cycles in our simulations; Fig.
418 S1B).

419 The *observation* model defines the likelihood of the current environmental sensory inputs (i.e. the
420 population vector of place cell firing \mathbf{P} , where $p_i(\bar{\mathbf{x}}) = f(\bar{\mathbf{x}} | \boldsymbol{\mu}_i, \boldsymbol{\Sigma}_{PC}^i)$ is the firing rate distribution of
421 place cell i over physical space $\bar{\mathbf{x}}$) given the predicted *metric* location \mathbf{x} , via a thresholded weighted
422 sum: $H(\mathbf{P} | \mathbf{x}) = [\sum_i B_i(\mathbf{x})P_i]^+$. Here, $B_i(\mathbf{x})$ is the location distribution of landmark i in *metric* space,
423 which would be encoded biophysically in the learned $[N_p \times N_g]$ matrix \mathbf{B} of synaptic weights from
424 place to grid cells (i.e. the g^{th} row and i^{th} column of \mathbf{B} is the distribution $B_i(\cdot)$ evaluated at the
425 location of the g^{th} grid cell). The normalization constant $K = \int G(\mathbf{x})d\mathbf{x}$ in Eq. 2 simply sums over
426 the current grid cell activity and might biophysically be implemented by inhibitory interneurons.

427 *Online learning of structural priors*

428 In the *online* model, the place-grid cell weight matrix \mathbf{B} is learned using the BCM rule:

429
$$\mathbf{B} \leftarrow \mathbf{B} + \tau_{PG} \mathbf{P}^\top \otimes [\mathbf{G}' \odot (\mathbf{G}' - \boldsymbol{\theta})] \quad (8a)$$

$$\boldsymbol{\theta} \leftarrow \boldsymbol{\theta} + \tau_\theta [(\mathbf{G} \odot \mathbf{G}) - \boldsymbol{\theta}] \quad (8b)$$

430 where $\tau_{PG} = 1e - 4$ is the learning rate and \mathbf{G}' and \mathbf{H} are column vectors whose elements are the
431 *transition* and *observation* models estimated at the locations of a finite set of grid cell locations. \odot is
432 the element-wise (Hadamard) product between two vectors and \otimes is their outer product. The sliding
433 threshold $\boldsymbol{\theta} \in R^{1 \times N_G}$ provides adaptive synaptic normalization, where $\tau_\theta \approx 10\tau_{PG}$. Learning takes
434 place between the *apriori* distribution \mathbf{G}' and the current sensory observation \mathbf{H} (i.e. before the
435 observation correction to \mathbf{G}').

436 *The offline probabilistic graphical model*

437 The pairwise potentials $\psi(\mathbf{b}_i - \mathbf{b}_j, \boldsymbol{\alpha} | \delta_{ij}) = \sum_{m,n=-\infty}^{\infty} \exp(-w_{ij}(\delta_{ij} - d_{mn}(\mathbf{b}_i - \mathbf{b}_j, \boldsymbol{\alpha}))^2)$ penalize
438 differences in the pairwise distances encoded by *association* δ_{ij} , and those that would be computed by
439 comparing their absolute encodings in *metric* space $d_{mn}(\cdot)$; i.e. they encourage a metric embedding
440 that reflects the associative distance. The *metric* distance function $d_{mn}^2(\mathbf{x}, \boldsymbol{\alpha}) = (\mathbf{x} + \mathbf{c}_{mn})^\top \boldsymbol{\alpha} (\mathbf{x} +$
441 $\mathbf{c}_{mn})$ defines the pairwise distance between the encoding of locations i and j in mEC in *metric* space,
442 and is dependent on the gain factor $\boldsymbol{\alpha}$ of the *transition model*. Pairwise measurements are assumed to
443 have confidence w_{ij} (inverse variance) that increases with decreasing inferred distance (i.e. $w_{ij} =$
444 $1/(\sigma_{PC} + \sigma_{PI}\delta_{ij})$). The *transition model* gain is assumed to have a Gaussian prior $p(\boldsymbol{\alpha}) =$
445 $\exp(-w_\alpha(\boldsymbol{\alpha} - \boldsymbol{\alpha}_0)^\top(\boldsymbol{\alpha} - \boldsymbol{\alpha}_0))$, the w_α term representing the confidence in the prior gain value $\boldsymbol{\alpha}_0$.
446 The periodic offset term \mathbf{c}_{mn} is the same as defined for the transition model.

447 *Associative encoding in the hippocampus*

448 The associative distances are recovered from the $[N_P \times N_p]$ synaptic weights in CA3 \mathbf{A} . Under a
449 random-walk behavioural trajectory, the simple modified Hebbian learning rule:

450
$$\mathbf{A} \leftarrow \mathbf{A} + \tau_{PP} [\mathbf{P} \mathbf{P}^\top - \mathbf{A} \odot \mathbf{A}] \quad (9)$$

451 where \odot is the element-wise (Hadamard) product and τ_{PP} the learning rate. The synaptic weights can
452 be shown to converge to $A_{ij} = \sqrt{\langle P_i(t)P_j(t) \rangle_t}$, the square-root of the correlation between the firing
453 rates of two PCs⁷⁰. Where place fields have uniform receptive field widths (σ_{PC}) and peak firing rates,
454 the Euclidean distance between place fields i and j can be inferred via the simple transformation⁴⁶:

$$455 \quad \delta_{ij}^2 = -\log(A_{ij}) = \frac{(\mu_i - \mu_j)^2}{2\sigma_{PC}^2} \quad (10)$$

456 The recovered distance is therefore scaled by the receptive fields' variance (the Bhattacharyya
457 distance⁴⁶), and so relates to 'discriminability' (Fig. 1D). CA3 synapses effectively average over
458 multiple pairwise measurements. By assuming that noise in the pairwise distance measurements scale
459 linearly with distance, both the mean and variance of the Gaussian describing this distribution is
460 efficiently encoded in a single PC-PC synapse.

461 Simplified analysis of the probabilistic graphical model likelihood

462 To characterize model predictions in the environmental rescaling⁷¹ and gain change⁷ experiments, we
463 studied a reduced version of the full graphical model (Eq. 3; see Supplementary Methods for full
464 derivation). In 1D, given a linear *observation model* $x = H(x') = K_1 + Kx'$ and a large number of
465 evenly spaced place fields, Eq. 3 simplifies to (see Supplementary Methods):

$$466 \quad -\log L = \ell \propto (1/\alpha^{visual} - K/\alpha)^2 + P_C(K - K^0)^2 + P_C \cdot T_C(1/\alpha - 1/\alpha^0)^2 \quad (11)$$

467 which can be solved analytically. A similar reduction was applied to the 2D case when considering
468 differential shifts in grid and place fields²³.

469 Belief propagation for *offline* inference

470 Belief propagation⁴⁸ is an iterative, two-stage local message-passing scheme in which, at each
471 iteration n , a feature node (i.e. a place cell) first updates its own belief (connections to the grid cells)
472 $B_i^{(n)}$ by integrating messages from connected nodes $j \in \Gamma_i$ with its own prior belief $B_i^{(0)}$ (Fig. 5C):

$$473 \quad B_i^{(n)}(\mathbf{b}_i) \propto B_i^{(0)}(\mathbf{b}_i) \prod_{j \in \Gamma_i} m_{j \rightarrow i}^{(n)}(\mathbf{b}_i) \quad (12a)$$

474 The message from node j to node i ($m_{j \rightarrow i}$) communicates its belief over the distribution of the
475 locations of place cell i in grid cell space, conditioned on its own location distribution:

476

$$m_{j \rightarrow i}^{(n+1)}(\mathbf{b}_i) \propto \int \psi(\mathbf{b}_j - \mathbf{b}_i, \boldsymbol{\alpha} | \delta_{ji}) \cdot \left[\frac{B_j^{(n)}(\mathbf{b}_j)}{m_{i \rightarrow j}^{(n)}(\mathbf{b}_j)} \right] d\mathbf{b}_j \quad (12b)$$

477 where the pairwise potentials $\psi(\cdot)$ are the same as those described in the full likelihood function (Eq.
478 3). The graph converges when new messages cease to change the beliefs of their recipient nodes.

479 Scheduled message passing on the place cell graph

480 ‘Synchronous’ belief propagation computes belief updates for each step before broadcasting all new
481 messages in the next step. In simulations, we demonstrated that scheduling message broadcasts based
482 on internal ‘message tension’ (divergence between previous and updated belief given new messages)
483 produced faster and more accurate convergence (Fig. 6B; see also Elidan et al.⁴⁹). Message tension
484 between the node’s previous $B_i^{(n-1)}$ and updated $B_i^{(n)}$ beliefs is defined as:

485

$$\mathcal{T}_i^n = \mathbb{JS}(B_i^{(n)} \parallel B_i^{(n-1)}) = \frac{1}{2} [\mathbb{KL}(B_i^{(n)} \parallel m) + \mathbb{KL}(B_i^{(n-1)} \parallel m)] \quad (13)$$

486 where \mathbb{JS} is the Jensen-Shannon (symmetric K-L) divergence, where:

487

$$m = \frac{1}{2} (B_i^{(n)} + B_i^{(n-1)})$$
$$\mathbb{KL}(p \parallel q) = - \int p(x) \cdot \log \left(\frac{q(x)}{p(x)} \right) dx \quad (14)$$

488 When the message tension is below a pre-defined threshold \mathcal{T}_{min} , a node has converged and ceases to
489 broadcast new messages. This mechanism is similar to the prediction error between *transition* and
490 *observation* models used to trigger *offline* inference, with the exception that it uses the symmetric
491 divergence measure \mathbb{JS} rather than \mathbb{KL} .

492 Traveling waves in neural media

493 In simulations, the traveling waves in mEC are simulated explicitly by calculating the true messages
494 conditioned on the sending nodes’ current beliefs at each time-step (Eq. 5B). In the ‘neural model’

495 (Fig. 7), messages were approximated as waves propagating radially from an initial stimulation on the
496 mEC sheet using a modified mechanical wave model, as used to describe oscillations in water:

497

$$\frac{d\boldsymbol{v}^2}{dt} = c^2 \nabla'^2 \cdot [\boldsymbol{v}]^+ \quad (15)$$

498 where c is the speed of wave propagation, $[\cdot]^+$ is a threshold linear activation function, and the
499 modified spatial Laplacian operator ∇' is a symmetric 2D Gaussian filter with variance equal to the PI
500 noise (see Supplementary Methods for extended discussion).

501 **Acknowledgements**

502 We thank the groups of Caswell Barry and Francesca Cacucci for use of their data and Martin Pearson
503 (UWE and Bristol Robotics Lab), Dan Bush, Andrej Bicanski and Tim Behrens for valuable
504 theoretical discussions.

505 We acknowledge funding by the ERC Advanced grant NEUROMEM, the Wellcome Trust and the
506 European Union's Horizon 2020 research and innovation programme under grant agreement
507 No. 785907 Human Brain Project SGA2. The authors declare no competing financial interests.

508 **References**

- 509 1. Burak, Y. & Fiete, I. R. Accurate path integration in continuous attractor network models of grid
510 cells. *PLoS computational biology* **5**, e1000291 (2009).
- 511 2. Fuhs, M. C. & Touretzky. A Spin Glass Model of Path Integration in Rat Medial Entorhinal
512 Cortex. *Journal of Neuroscience* **26**, 4266–4276 (2006).
- 513 3. McNaughton, B. L., Battaglia, F. P., Jensen, O., Moser, E. I. & Moser, M.-B. Path integration and
514 the neural basis of the ‘cognitive map’. *Nature Reviews Neuroscience* **7**, 663–678 (2006).
- 515 4. Lever, C., Burton, S., Jeewajee, A., O’Keefe, J. & Burgess, N. Boundary Vector Cells in the
516 Subiculum of the Hippocampal Formation. *Journal of Neuroscience* **29**, 9771–9777 (2009).
- 517 5. Hartley, T., Burgess, N., Lever, C., Cacucci, F. & O’keefe, J. Modeling place fields in terms of
518 the cortical inputs to the hippocampus. *Hippocampus* **10**, 369–379 (2000).

- 519 6. O'Keefe, J. & Burgess, N. Dual phase and rate coding in hippocampal place cells: Theoretical
520 significance and relationship to entorhinal grid cells. *Hippocampus* **15**, 853–866 (2005).
- 521 7. Chen, G., Lu, Y., King, J. A., Cacucci, F. & Burgess, N. Differential influences of environment
522 and self-motion on place and grid cell firing. *Nature communications* **10**, 630 (2019).
- 523 8. Hardcastle, K., Ganguli, S. & Giocomo, L. M. Environmental Boundaries as an Error Correction
524 Mechanism for Grid Cells. *Neuron* (2015) doi:10.1016/j.neuron.2015.03.039.
- 525 9. Keinath, A. T., Epstein, R. A. & Balasubramanian, V. Environmental deformations dynamically
526 shift the grid cell spatial metric. *eLife* **7**, e38169 (2018).
- 527 10. Durrant-Whyte, H. & Bailey, T. Simultaneous localization and mapping: part I. *IEEE Robotics &*
528 *Automation Magazine* **13**, 99–110 (2006).
- 529 11. Milford, M. J., Wyeth, G. F. & Prasser, D. RatSLAM: a hippocampal model for simultaneous
530 localization and mapping. in *Robotics and Automation, 2004. Proceedings. ICRA '04. 2004 IEEE*
531 *International Conference on* vol. 1 403–408 (IEEE, 2004).
- 532 12. Guo, W., Zhang, J. J., Newman, J. & Wilson, M. A. Latent learning drives sleep-dependent
533 plasticity in distinct CA1 subpopulations. *bioRxiv* (2020).
- 534 13. Ocko, S. A., Hardcastle, K., Giocomo, L. M. & Ganguli, S. Emergent elasticity in the neural code
535 for space. *Proceedings of the National Academy of Sciences* **115**, E11798–E11806 (2018).
- 536 14. Penny, W. D., Zeidman, P. & Burgess, N. Forward and backward inference in spatial cognition.
537 *PLoS computational biology* **9**, e1003383 (2013).
- 538 15. Evans, T. & Burgess, N. Coordinated hippocampal-entorhinal replay as structural inference. in
539 *Advances in Neural Information Processing Systems* (2019).
- 540 16. Diba, K. & Buzsáki, G. Forward and reverse hippocampal place-cell sequences during ripples.
541 *Nature Neuroscience* **10**, 1241–1242 (2007).
- 542 17. Foster, D. J. & Wilson, M. A. Reverse replay of behavioural sequences in hippocampal place
543 cells during the awake state. *Nature* **440**, 680–683 (2006).
- 544 18. Ólafsdóttir, H. F., Carpenter, F. & Barry, C. Coordinated grid and place cell replay during rest.
545 *Nature Neuroscience* **19**, 792–794 (2016).

- 546 19. O'Neill, J., Boccaro, C., Stella, F., Schoenenberger, P. & Csicsvari, J. Superficial layers of the
547 medial entorhinal cortex replay independently of the hippocampus. *Science* **355**, 184–188 (2017).
- 548 20. Wilson, M. A. & McNaughton, B. L. Dynamics of the hippocampal ensemble code for space.
549 *Science* **261**, 1055–1058 (1993).
- 550 21. Barry, C., Hayman, R., Burgess, N. & Jeffery, K. J. Experience-dependent rescaling of entorhinal
551 grids. *Nature Neuroscience* **10**, 682–684 (2007).
- 552 22. Barry, C., Ginzberg, L. L., O'Keefe, J. & Burgess, N. Grid cell firing patterns signal
553 environmental novelty by expansion. *Proceedings of the National Academy of Sciences* **109**,
554 17687–17692 (2012).
- 555 23. Krupic, J., Bauza, M., Burton, S. & O'Keefe, J. Local transformations of the hippocampal
556 cognitive map. *Science* **359**, 1143–1146 (2018).
- 557 24. Stensola, H. *et al.* The entorhinal grid map is discretized. *Nature* **492**, 72–78 (2012).
- 558 25. Butler, W. N., Hardcastle, K. & Giocomo, L. M. Remembered reward locations restructure
559 entorhinal spatial maps. *Science* **363**, 1447–1452 (2019).
- 560 26. Hägglund, M., Mørreaut, M., Moser, M.-B. & Moser, E. I. Grid-Cell Distortion along
561 Geometric Borders. *Current Biology* (2019) doi:10.1016/j.cub.2019.01.074.
- 562 27. Hollup, S. A., Molden, S., Donnett, J. G., Moser, M.-B. & Moser, E. I. Accumulation of
563 hippocampal place fields at the goal location in an annular watermaze task. *Journal of
564 Neuroscience* **21**, 1635–1644 (2001).
- 565 28. Munn, R. G. K., Mallory, C. S., Hardcastle, K., Chetkovich, D. M. & Giocomo, L. M. Entorhinal
566 velocity signals reflect environmental geometry. *bioRxiv* (2019) doi:10.1101/671222.
- 567 29. Stensola, T., Stensola, H., Moser, M.-B. & Moser, E. I. Shearing-induced asymmetry in
568 entorhinal grid cells. *Nature* **518**, 207–212 (2015).
- 569 30. Hafting, T., Fyhn, M., Molden, S., Moser, M.-B. & Moser, E. I. Microstructure of a spatial map
570 in the entorhinal cortex. *Nature* **436**, 801–806 (2005).
- 571 31. Fiete, I. R., Burak, Y. & Brookings, T. What Grid Cells Convey about Rat Location. *Journal of
572 Neuroscience* **28**, 6858–6871 (2008).

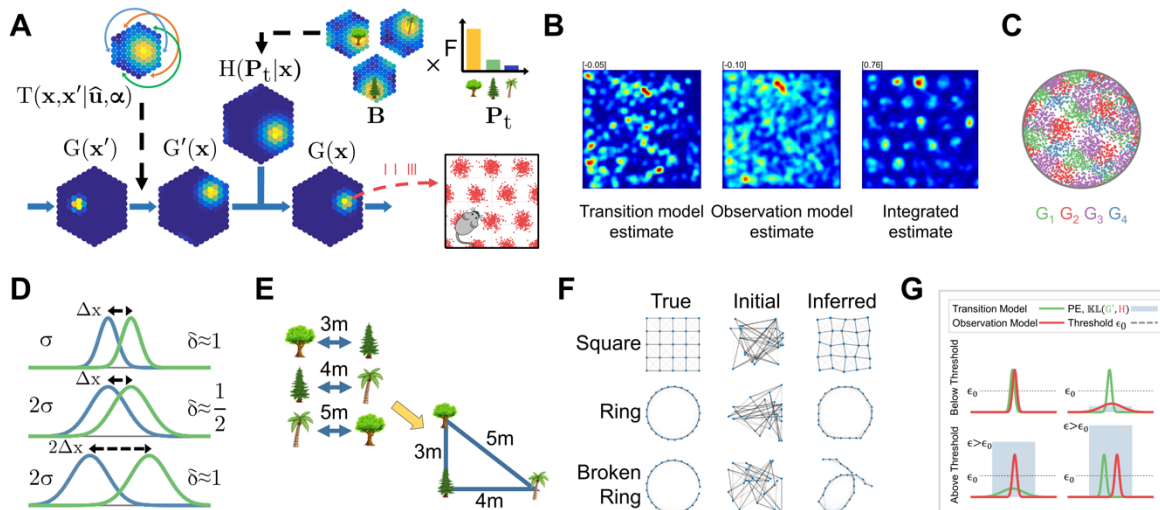
- 573 32. Mathis, A., Herz, A. V. & Stemmler, M. Optimal population codes for space: grid cells
574 outperform place cells. *Neural computation* **24**, 2280–2317 (2012).
- 575 33. Stemmler, M., Mathis, A. & Herz, A. V. M. Connecting multiple spatial scales to decode the
576 population activity of grid cells. *Science Advances* **1**, e1500816–e1500816 (2015).
- 577 34. Guanella, A., Kiper, D. & Verschure, P. A model of grid cells based on a twisted torus topology.
578 *International journal of neural systems* **17**, 231–240 (2007).
- 579 35. Stachenfeld, K. L., Botvinick, M. M. & Gershman, S. J. The hippocampus as a predictive map.
580 *Nature Neuroscience* (2017) doi:10.1038/nn.4650.
- 581 36. Whittington, J., Muller, T., Mark, S., Barry, C. & Behrens, T. Generalisation of structural
582 knowledge in the hippocampal-entorhinal system. in *Advances in Neural Information Processing*
583 *Systems 31* (eds. Bengio, S. et al.) 8484–8495 (Curran Associates, Inc., 2018).
- 584 37. Widloski, J. & Fiete, I. R. A Model of Grid Cell Development through Spatial Exploration and
585 Spike Time-Dependent Plasticity. *Neuron* **83**, 481–495 (2014).
- 586 38. Kropff, E., Carmichael, J. E., Moser, M.-B. & Moser, E. I. Speed cells in the medial entorhinal
587 cortex. *Nature* **523**, 419–424 (2015).
- 588 39. Munn, R. G. K., Mallory, C. S., Hardcastle, K., Chetkovich, D. M. & Giocomo, L. M. Entorhinal
589 velocity signals reflect environmental geometry. *Nat Neurosci* (2020) doi:10.1038/s41593-019-
590 0562-5.
- 591 40. Milford, M. J. & Wyeth, G. F. Mapping a suburb with a single camera using a biologically
592 inspired SLAM system. *IEEE Transactions on Robotics* **24**, 1038–1053 (2008).
- 593 41. Muller, R. U., Stead, M. & Pach, J. The hippocampus as a cognitive graph. *The Journal of*
594 *general physiology* **107**, 663–694 (1996).
- 595 42. Burgess, N. & O’Keefe, J. Neuronal computations underlying the firing of place cells and their
596 role in navigation. *Hippocampus* **6**, 749–762 (1996).
- 597 43. Campbell, M. G. *et al.* Principles governing the integration of landmark and self-motion cues in
598 entorhinal cortical codes for navigation. *Nature neuroscience* **21**, 1096 (2018).
- 599 44. Krupic, J., Bauza, M., Burton, S., Barry, C. & O’Keefe, J. Grid cell symmetry is shaped by
600 environmental geometry. *Nature* **518**, 232–235 (2015).

- 601 45. Hägglund, M. & Mørreaut, M. Grid pattern development, distortions and topological defects
602 may depend on distributed anchoring. *BioRxiv* 830158 (2019).
- 603 46. Bhattacharyya, A. On a measure of divergence between two statistical populations defined by
604 their probability distributions. *Bull. Calcutta Math. Soc.* **35**, 99–109 (1943).
- 605 47. Tanni, S. & Barry, C. Relationship between place cell recruitment and the spatial scale of open-
606 field environments revealed using a novel scalable recording apparatus. in *Society for*
607 *Neuroscience* Program No. 689.18. (Society for Neuroscience, 2018).
- 608 48. Pearl, J. Reverend Bayes on inference engines: A distributed hierarchical approach. in *National*
609 *Conference on Artificial Intelligence* 133–136 (AII Press, 1982).
- 610 49. Elidan, G., McGraw, I. & Koller, D. Residual belief propagation: Informed scheduling for
611 asynchronous message passing. *arXiv preprint arXiv:1206.6837* (2012).
- 612 50. Davidson, T. J., Kloosterman, F. & Wilson, M. A. Hippocampal Replay of Extended Experience.
613 *Neuron* **63**, 497–507 (2009).
- 614 51. Stella, F., Baracskay, P., O'Neill, J. & Csicsvari, J. Hippocampal Reactivation of Random
615 Trajectories Resembling Brownian Diffusion. *Neuron* (2019) doi:10.1016/j.neuron.2019.01.052.
- 616 52. Bellmund, J. L. *et al.* Deforming the metric of cognitive maps distorts memory. *Nature human*
617 *behaviour* 1–12 (2019).
- 618 53. Boccara, C. N., Nardin, M., Stella, F., O'Neill, J. & Csicsvari, J. The entorhinal cognitive map is
619 attracted to goals. *Science* **363**, 1443–1447 (2019).
- 620 54. Nakazawa, K. *et al.* Requirement for hippocampal CA3 NMDA receptors in associative memory
621 recall. *Science* **297**, 211–218 (2002).
- 622 55. Dordek, Y., Soudry, D., Meir, R. & Derdikman, D. Extracting grid cell characteristics from place
623 cell inputs using non-negative principal component analysis. *eLife* **5**, (2016).
- 624 56. Banino, A. *et al.* Vector-based navigation using grid-like representations in artificial agents.
625 *Nature* **557**, 429 (2018).
- 626 57. Carpenter, F., Manson, D., Jeffery, K., Burgess, N. & Barry, C. Grid Cells Form a Global
627 Representation of Connected Environments. *Current Biology* 1–7 (2015)
628 doi:10.1016/j.cub.2015.02.037.

- 629 58. Lee, A. K. & Wilson, M. A. Memory of sequential experience in the hippocampus during slow
630 wave sleep. *Neuron* **36**, 1183–1194 (2002).
- 631 59. Skaggs, W. E. & McNaughton, B. L. Replay of neuronal firing sequences in rat hippocampus
632 during sleep following spatial experience. *Science* **271**, 1870–1873 (1996).
- 633 60. Wilson, M. A. & McNaughton, B. L. Reactivation of hippocampal ensemble memories during
634 sleep. *Science* **265**, 676–679 (1994).
- 635 61. Buzsáki, G., Vanderwolf, C. H. & others. Cellular bases of hippocampal EEG in the behaving rat.
636 *Brain Research Reviews* **6**, 139–171 (1983).
- 637 62. O’Keefe, J. Place units in the hippocampus of the freely moving rat. *Experimental neurology* **51**,
638 78–109 (1976).
- 639 63. Bicanski, A. & Burgess, N. A neural-level model of spatial memory and imagery. *eLife* **7**, e33752
640 (2018).
- 641 64. Mattar, M. G. & Daw, N. D. Prioritized memory access explains planning and hippocampal
642 replay. (2018) doi:10.1101/225664.
- 643 65. Momennejad, I., Otto, A. R., Daw, N. D. & Norman, K. A. Offline replay supports planning in
644 human reinforcement learning. *Elife* **7**, e32548 (2018).
- 645 66. Hasselmo, M. E. Neuronal rebound spiking, resonance frequency and theta cycle skipping may
646 contribute to grid cell firing in medial entorhinal cortex. *Philosophical Transactions of the Royal
647 Society of London B: Biological Sciences* **369**, 20120523 (2014).
- 648 67. Muller, L., Chavane, F., Reynolds, J. & Sejnowski, T. J. Cortical travelling waves: mechanisms
649 and computational principles. *Nature Reviews Neuroscience* (2018).
- 650 68. Yamamoto, J. & Tonegawa, S. Direct medial entorhinal cortex input to hippocampal CA1 is
651 crucial for extended quiet awake replay. *Neuron* **96**, 217–227 (2017).
- 652 69. Mathis, A., Stemmler, M. B. & Herz, A. V. Probable nature of higher-dimensional symmetries
653 underlying mammalian grid-cell activity patterns. *Elife* **4**, e05979 (2015).
- 654 70. Dayan, P. & Abbott, L. F. *Theoretical neuroscience*. (Cambridge, MA: MIT Press, 2001).
- 655 71. Barry, C. & Burgess, N. Learning in a geometric model of place cell firing. *Hippocampus* **17**,
656 786–800 (2007).

657

658 **Figure 1.** Online+offline localization and mapping. **A)** Illustration of recursive Bayesian
 659 integration. A probability distribution over current location ($G(x)$), represented by grid cell
 660 firing, is updated according to self-motion via the *transition model* ($T(x, x' | \hat{u}, \alpha)$) then refined
 661 by environmental inputs via the *observation model* ($H(P_t | x_t)$). **C)** Estimates based on the
 662 integration of noisy self-motion and environmental inputs may be stable, as shown in
 663 simulated grid cell firing rate maps (*right*), despite instability when using only self-motion
 664 (*left*) or environmental inputs after brief initial exploration (*middle*; numbers show gridness
 665 score). **C)** Simulated grid cells exhibit spatially offset grid-like firing patterns, due to toroidal
 666 connectivity, despite the absence of attractor dynamics. Right shows histogram of spatial
 667 phases. **D)** Inferred pairwise distances D are a function of the ‘overlap’ between place fields.
 668 **E)** Pairwise distances can be used to infer the structure of the world (the mapping of place
 669 fields onto the grid map). **F)** Given noisy initial priors (“Initial”), structural encodings are
 670 modified to reflect pairwise *associative* measurements. Inferred structure is sensitive to the
 671 topology of the environment (cf. “Ring” and “Broken Ring”). **G)** Illustration of the prediction
 672 error mechanism used to arbitrate between the *online* and *offline* systems (blue bars show
 673 prediction error ϵ , ϵ_0 is the minimum prediction error needed to trigger *offline* inference).



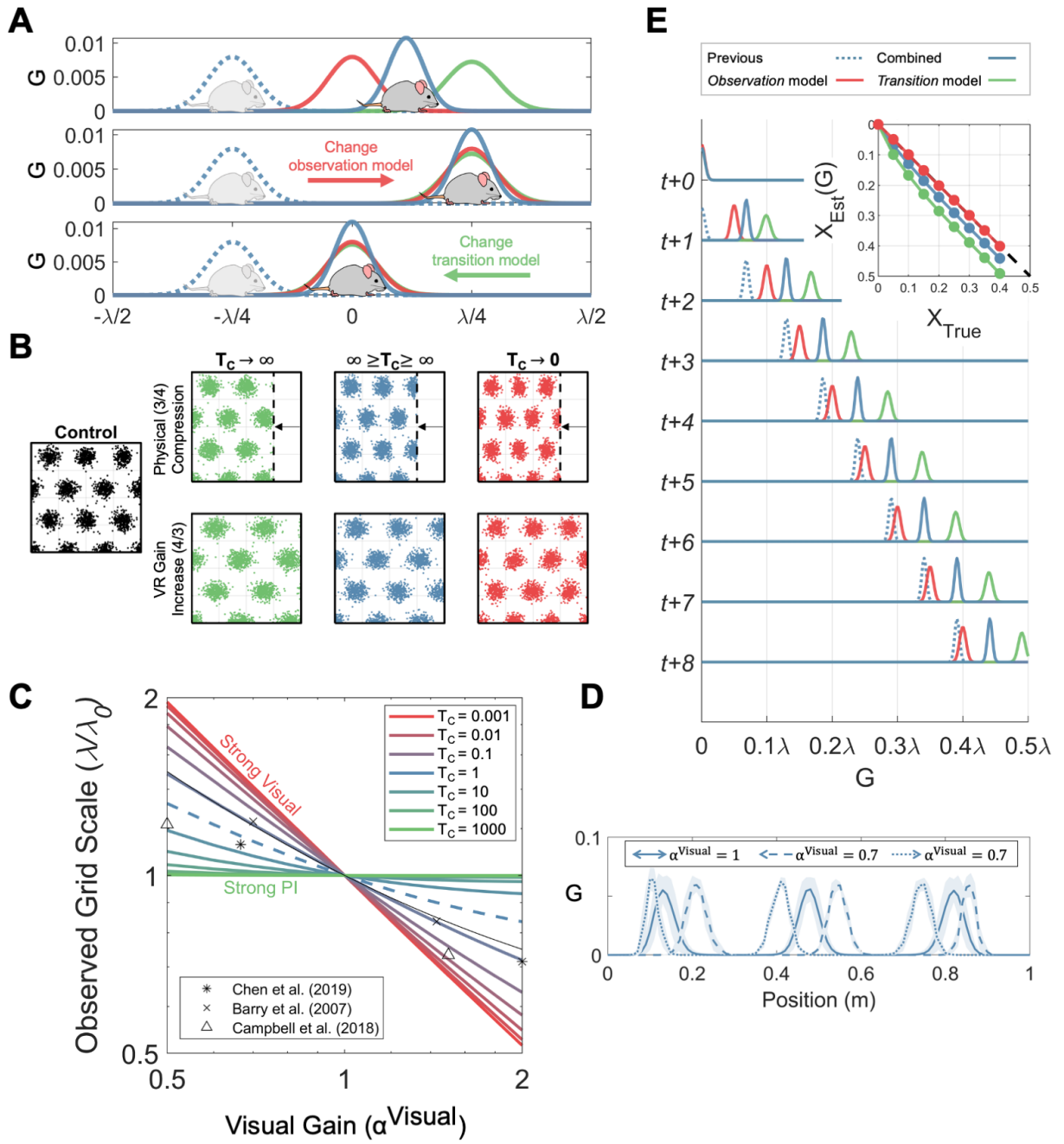
674

675

676

677 **Figure 2.** Minimizing prediction errors in the *offline* system: grid rescaling and direction-
678 dependent offsets under manipulations of environmental size or VR gain. **A)** During *online*
679 spatial localization, the *observation* model estimates location in metric space (activity on the
680 grid sheet) via inputs from place cells driven by environmental features (red curve), the
681 *transition* model updates the previous estimate (dashed blue curve) according to self-motion
682 (green curve), producing a combined estimate (blue curve). Manipulations of the
683 environment cause the predictions from both models to diverge. One way to minimize these
684 prediction errors is to modify the *observation* model by changing the connection weights
685 from place to grid cells (i.e. the mapping between environmental observations to estimated
686 location in grid space). An alternative is to modify the *transition* model to reflect the
687 *observation* model estimate (e.g. varying the ‘gain’ mapping self-motion to grid space). The
688 degree to which both are modified is controlled by the relative strength of their respective
689 prior confidences (T_C). **B)** Joint optimization of the *observation* and *transition* models predict
690 partial rescaling of grid patterns in response to increase in the VR gain (i.e. the rate of visual
691 movement in response to physical movement on the ball; below) or compression of a real
692 environment (above). When the system is confident in its self-motion ($T_C \rightarrow \infty$, green), the
693 *observation* model is modified to match the *transition* model (no change in grid scale plotted
694 in the real or visual VR environment). When the system is confident in its environmental
695 inputs ($T_C \rightarrow 0$, red), the *transition* model adapts and grid scale follows the environmental
696 change. Balanced model confidence produces intermediate rescaling (blue). **C)** Change in
697 observed grid scale (grid pattern plotted against self-motion) depends on the *transition*
698 confidence values T_C . X-axis shows VR gain change or environmental compression, where
699 $\alpha^{\text{Visual}} = 1$ is a control trial. Y-axis shows observed change in grid scale (see Methods). Data
700 points show corresponding values from Barry et al. (2007), Chen et al. (2019) and Campbell
701 et al., (2019), which suggest an approximately equal weighting of *transition* and *observation*
702 model priors for both gain decreases and increase trials ($T_C \approx 1$). **D)** Firing rate map of a grid
703 cell on the linear track in control (solid line) and VR gain decrease trials ($\alpha^{\text{Visual}} = 0.7$),

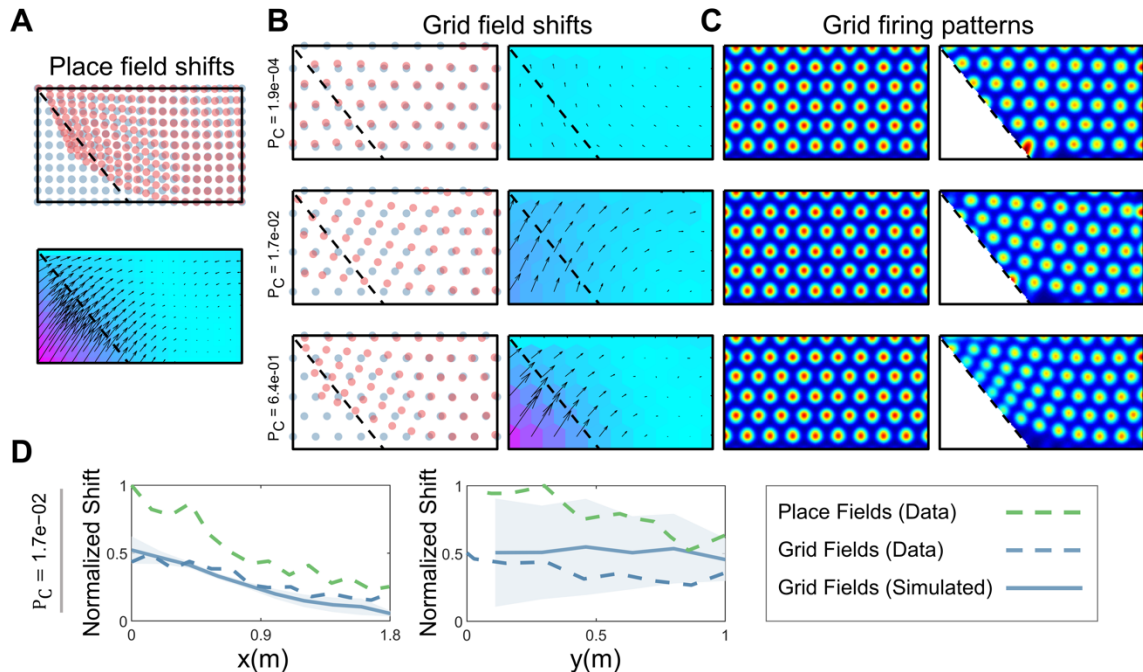
704 plotted in the visual VR environment. In the gain decrease condition, the grid fields are stably
705 shifted to fire earlier when running left (dashed line) or right (dotted line), i.e. towards the
706 location indicated by the transition model from that indicated by vision. **E)** The direction-
707 dependent shift in estimated location in the grid module in a VR gain decrease trial
708 ($\alpha^{Visual} = \frac{2}{3}$) stabilises at a fixed distance. Sequence of eight updates of estimated location
709 on the grid module G(x) when running to the right in a VR visual gain decrease trial, colours
710 as in A. The *transition* model (green) predicts a location ahead of that from the *observation*
711 model on the grid sheet (red; driven by visual input) because of the visual gain decrease.
712 Combining these estimates produces an intermediate distribution (blue). At each new
713 update, the prediction from the *transition* model builds on the shift of the previous combined
714 estimate (not the previous transition model estimate) so that the distance between the
715 observation model estimate and the combined estimate stabilizes at a fixed value, producing
716 a fixed direction-dependent offset of the grid patterns in environmental coordinates (see the
717 differences in the location estimates between models, Inset).



718

719

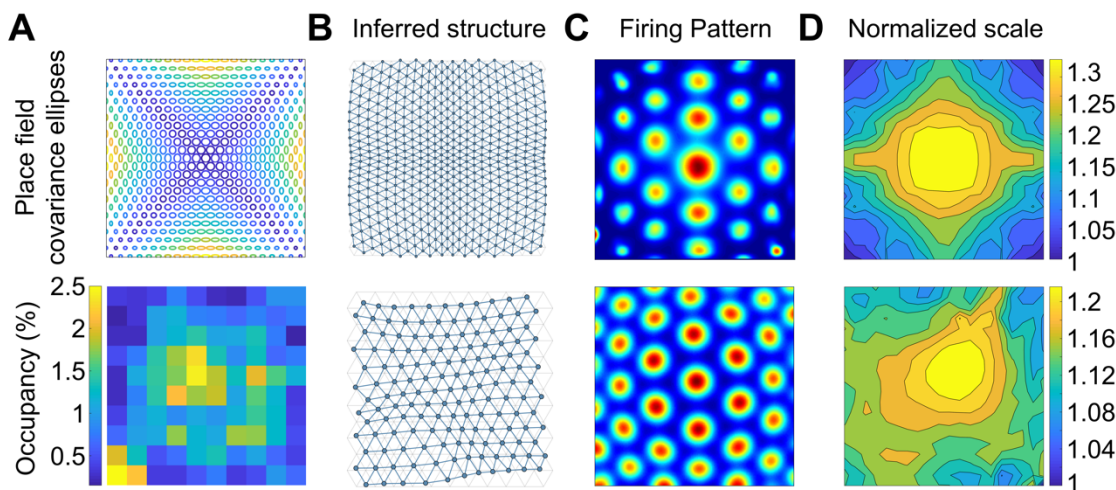
720 **Figure 3.** Effects of local deformation of a rectangular environment on grid patterns following
721 *offline* inference (Krupic et al., 2018). Dots indicate place/grid field locations, arrows indicate
722 shifts before/after *offline* structural optimization and coloured hexagons indicate magnitude
723 of shift vector. Grid patterns show estimate generated by the *observation* model (weighted
724 place cell activity). **A)** Place field shifts were measured from Krupic et al. (2018) and
725 interpolated and smoothed. **B-C)** Place field shifts cause immediate prediction errors (PE)
726 between the new pairwise place field distances and the distances between their
727 corresponding grid locations. If the *observation / transition* model priors are weak ($P_C \rightarrow 0$),
728 PEs are eliminated during *offline* inference by updating the *observation* model (top row;
729 unlike in Fig. 4B, modifying the global gain did not remove the effect of local distortions).
730 Complete adaptation in the *observation* model leads to an unperturbed grid pattern, i.e. grid
731 fields will not shift. Alternatively, strong model priors ($P_C \rightarrow \infty$) prevent adaptation to new
732 environmental inputs, leading to distorted grid patterns when driven purely by the
733 observation model, whose field shifts match those of the place cells (bottom row). When the
734 model priors are balanced against the new pairwise observations, the *observation* model is
735 partially adjusted, producing partial grid field shifts (which are smaller than those of the place
736 fields; middle row). Partial (middle) or no (bottom) adjustment to new observations preserve
737 mismatches between the *transition* and *observation* models, which would result in direction-
738 dependent offsets (see Figure 4E) and irregular firing patterns (see Figure S2D). NB the
739 confidence in the prior model may depend on location, e.g. if there is strong anchoring to the
740 wall prior connections from place cells with fields near the wall may be stronger than those
741 with fields further away. **D)** Comparison of experimentally observed place and grid field shifts
742 with simulation corresponding to the middle row of **B-C**.



743

744

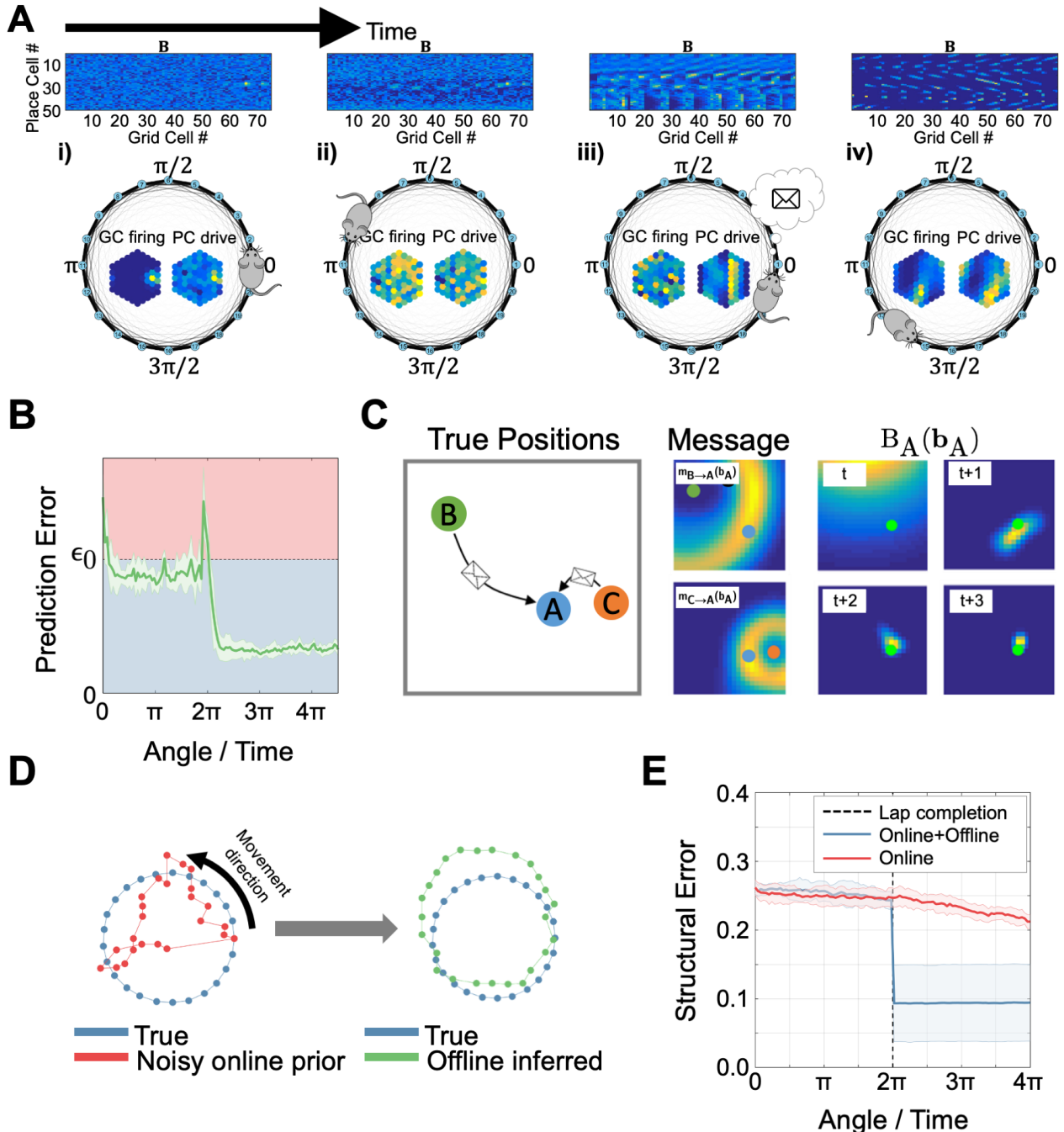
745 **Figure 4.** Distortions to grid patterns caused by inhomogeneous environmental input during
746 offline inference. **A)** Simulated variation in place field shape due to proximity to boundaries
747 (above), or inhomogeneous sampling of locations (Hagglund et al., 2019; below) results in
748 distortions to the inferred pairwise distances in CA3 (**B**). These distortions lead to distortions
749 to grid scale due to adjustment of the observation model during offline inference (**C-D**).



750

751

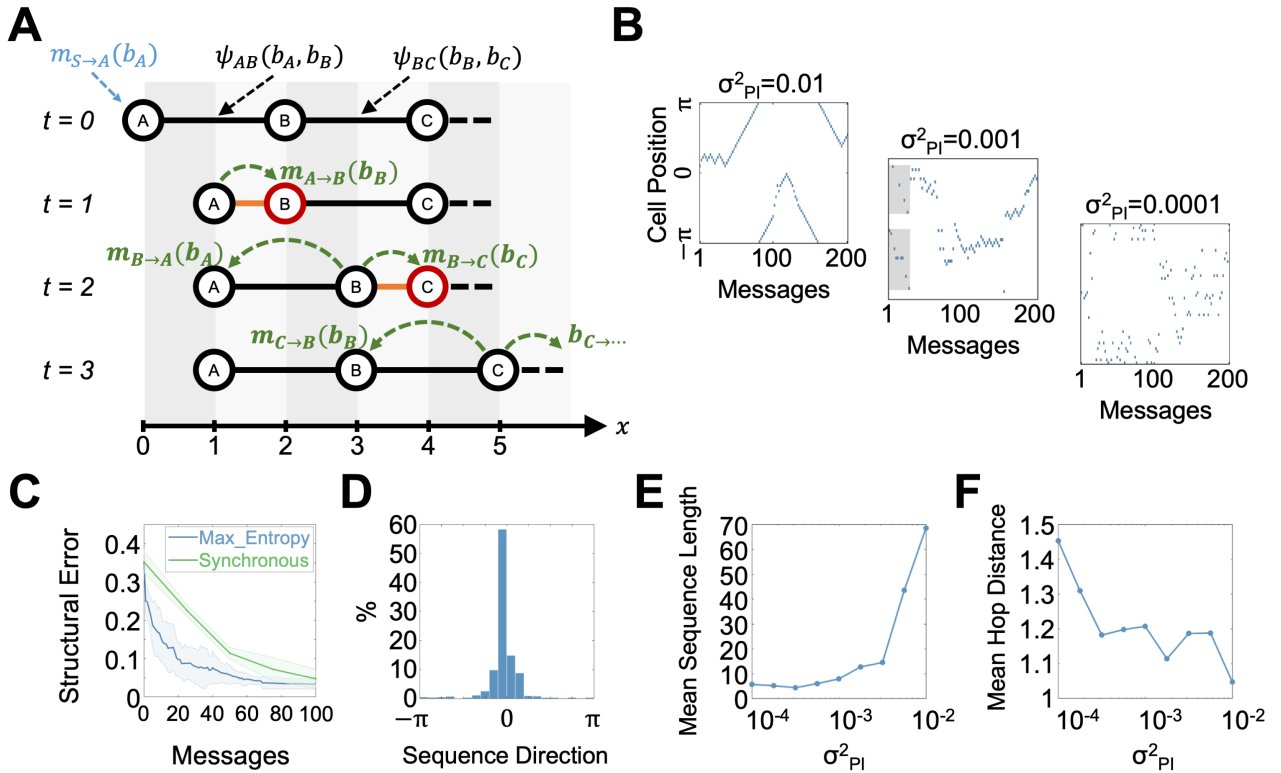
752 **Figure 5.** Illustration of the dual-systems model: prediction errors and replay in the loop-
753 closure task (see also Supplementary Video 1). **A)** Place cell – grid cell (PC-GC) connection
754 weights (above) as agent runs around a circular track for the first time (below, GC activity
755 and the input from PCs to GCs, both shown on topographically organised sheet of cells,
756 inset). **i)** Confidence in the initial location is high, such that coactive GC and PC fields form
757 strong associations (the GC firing distribution is peaked and the inputs from place cells with
758 fields at the beginning of the track are strong). **ii)** The agent navigates around the track,
759 accumulating self-motion error, leading to diffuse GC firing. **iii)** Prediction errors (PE) on lap
760 completion (when the initially learned precise PC input arrives) triggers an *offline* inference
761 event (see main text and Supp. Video 1 for details). **iv)** On subsequent laps of the track, PC-
762 GC weights are sharply tuned following *offline* inference, allowing effective localization. **B)**
763 PE is reduced on completion of subsequent laps due to alignment of the *transition* and
764 *observation models* (i.e. environmental inputs and self-motion updating of GC activity
765 coincide). **C)** Illustration of belief propagation. Place cell A receives messages from PCs B
766 and C. Messages take the form of rings, describing a preferred distance about the current
767 locations of B and C with variance reflecting the confidence in the message (the variance of
768 pairwise distance estimates with Gaussian noise). The intersection of the messages
769 uniquely determines the location of A over time. NB A will also be broadcasting messages
770 back to B and C. **D)** True structure (blue), structure encoded by noisy path integration (left,
771 red; i.e. the location of the peaks of the weights from each place cell to the grid cell sheet)
772 and structure inferred after loop-closure (right, green). **E)** *Offline* inference allows one-shot
773 learning when compared to the online system alone.



774

775

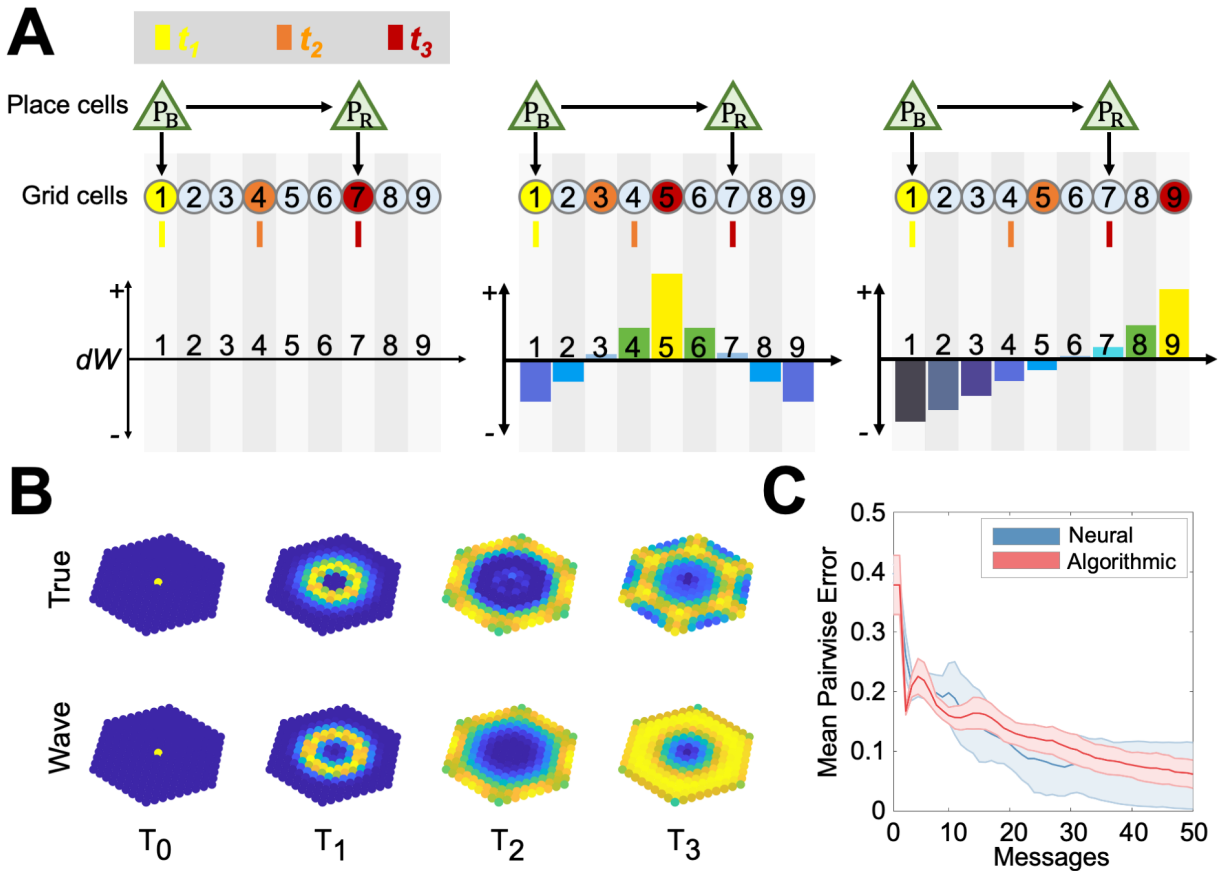
776 **Figure 6.** Principled message scheduling during *offline* inference generates sequences of
777 place cell activity. **A)** Place cells (i.e. graph nodes representing conjunctions of
778 environmental features) are connected via their pairwise potentials (ψ_{AB} , ψ_{BC}), which
779 penalize the mismatch between *associative* and *metric* pairwise distances (δ_{ij} and d_{ij}
780 respectively). ($t = 0$) Environmental sensory input ($m_{S \rightarrow A}(b_A)$) causes an update to the belief
781 of place cell A (i.e. updating its synaptic weights to the grid sheet) by making it fire in a new
782 location $b_A = 1$. ($t = 1$) Place cell A sends a message to B expressing its belief over the
783 location of B, given its own (new) location and the *associative* distance δ_{AB} , causing B to
784 update its belief. ($t = 2$) Messages from B to A and C only cause C to update its belief, so
785 only C broadcasts at the next time-step. **B)** Examples of PC reactivation sequences in loop-
786 closure task for different values of path integration noise σ_{PI}^2 (and therefore pairwise
787 measurement confidence, since $w_{ij} = 1/(\sigma_{PC}^2 + \sigma_{PI}^2 \delta_{ij})$; where $\sigma_{PC}^2 = 1e-4$). Multiple local
788 sequences can occur in interleaved fashion (Middle, grey shading) and become longer and
789 smoother when pairwise measurements are less confident (Right; also **E**, **F**). **C)** The 'Max-
790 Entropy' schedule (i.e., only the place cell with max entropy change fires in the next-step)
791 converges faster than when all PCs broadcast messages at each time-step. **D)** Forward and
792 reverse sequences occurred approximately equally often.



793

794

795 **Figure 7.** Schematic neural mechanism for probabilistic message passing (see also
796 Supplementary Video 2). **A)** Illustration in 1D. The broadcasting place cell P_B sends a spike
797 to receiving place cell P_R via recurrent connections in CA3, and also initiates a travelling
798 wave at the corresponding location on the grid cell module via their connections there. (Left)
799 No new learning occurs when the spike and travelling wave arrive at P_R and its
800 corresponding grid location (GC_7) at the same time, as P_R-GC_7 connection will already be
801 strong. (Middle) If the CA3 spike arrives at P_R ahead of the travelling wave reaching GC_7 , the
802 synaptic associations of P_R are adjusted towards the currently active GC_5 (updating the
803 belief, by increasing P_R-GC_5 and decreasing P_R-GC_7 , see dW , below). (Right) Same as
804 middle, except that GC wave reaches GC_7 before the CA3 spike reaches P_R . **B)** Propagating
805 messages as travelling waves in mEC. A neural simulation of travelling waves with a
806 modified Laplacian diffusion kernel (Wave) closely approximates the probabilistic
807 propagation of activity (True), reflecting the accumulation of self-motion noise in the
808 broadening of the wave front. **C)** Comparison of the algorithmic and neural belief
809 propagation performance.



810

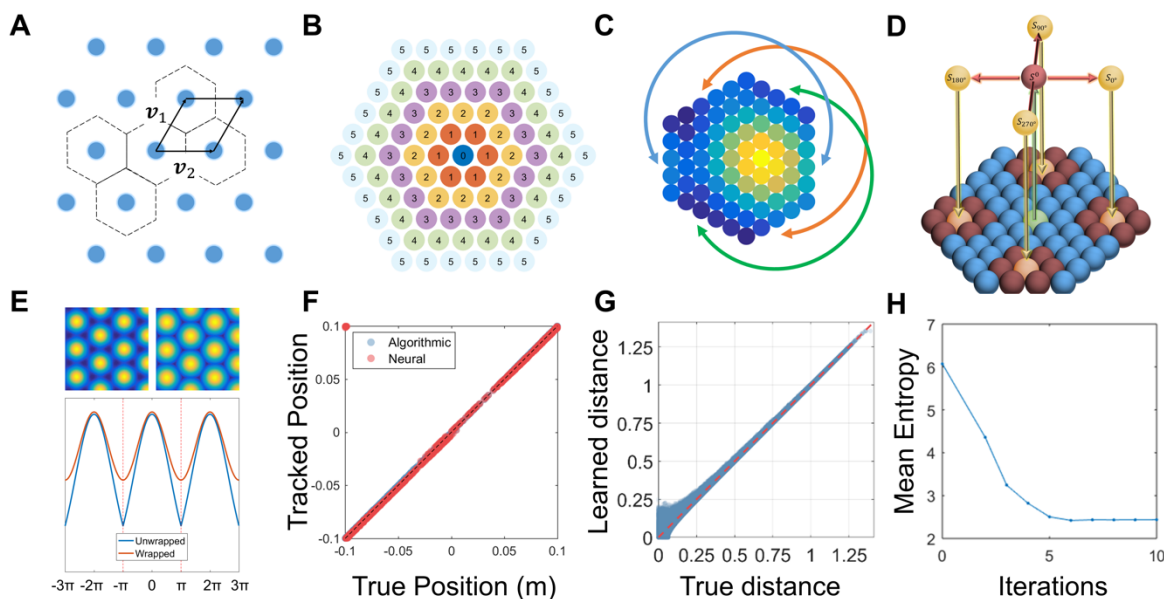
811

812

|

41

813 **Figure S1** Implementational details of the *online* system. **A** The mapping from real to grid
814 cell space can be considered as the subtraction of a mapping vector $[i \cdot \nu_1 + j \cdot \nu_2]$, where
815 each grid field can be described as a point on a 2D lattice with basis vectors ν_1 and ν_2 . Each
816 grid field has associated with it a Voronoi domain, defined as the region within which any
817 point is closest to the corresponding grid field. When mapping from grid-to-real space, the
818 vector of the closest grid field is subtracted. **B** The wrapped Normal distribution is a
819 summation of the likelihoods of the current position estimate being at any one of an infinite
820 number of periodic tilings (here, five wrappings are shown). **C** The grid cells are connected
821 periodically to produce a ‘twisted-torus’ topology. **D** Illustration of the shifter cell mechanism.
822 Each ‘readout’ grid cell is connected to four ‘shifter’ grid cells and a single self-connecting
823 cell. **E** Illustration of the difference between wrapped and non-wrapped Gaussian
824 distributions. **F** Correspondence between the neural shifter cell mechanism and the
825 algorithmic transition function. **G** Pairwise distances between place fields can be inferred
826 from the strengths of Hebbian connections. **H** Mean entropy in the beliefs of each place cell
827 over their encoded location in grid space (encoded in place-grid cell connection weight
828 distributions decreases with iterations during *offline* inference.



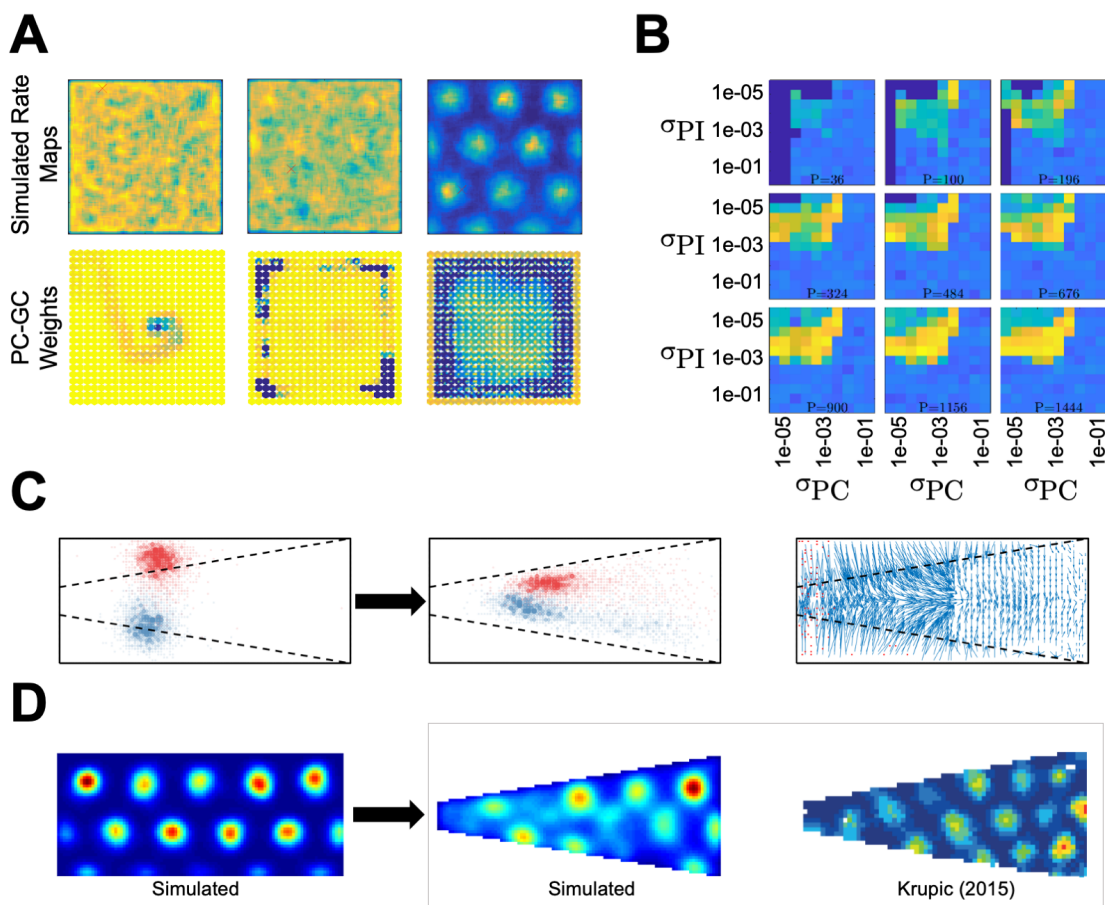
829

830

831

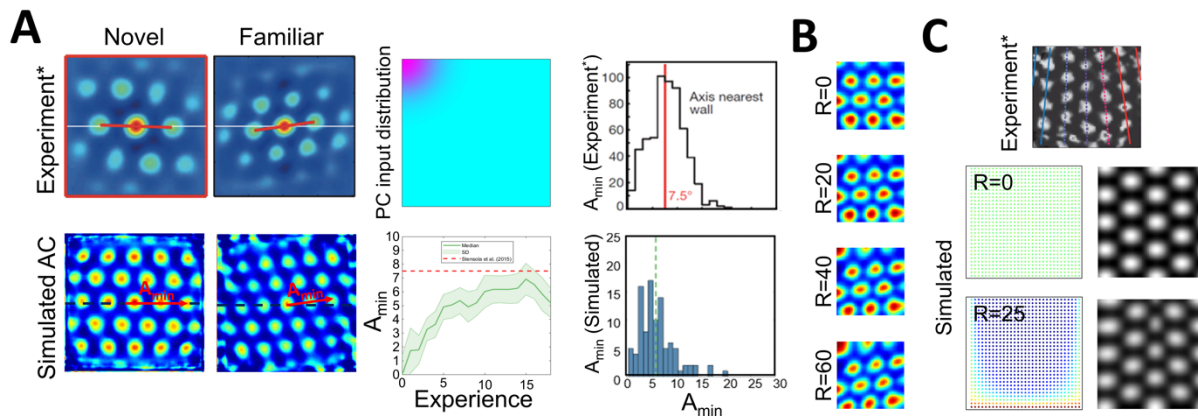
832

833 **Figure S2 A** Convergence of grid patterns and place-grid cell weights over three periods
834 (columns). The place-grid cell weights (*bottom row*, colour denotes normalized connection
835 strength) converge fastest near to the boundaries (as seen in development; Muessig et al.,
836 2015) and corners of an environment, since trajectories through are more directionally
837 constrained. Top row shows corresponding grid patterns (colour denotes normalized firing
838 rate). **B** Convergence of stable grid patterns over sensory noise (σ_{PC}) and path integration
839 noise (σ_{PI}). Colour denotes grid score (Sargolini et al., 2006). P indicates number of place
840 cells used in simulations. **C-D** Environmental deformations caused by prior structural beliefs.
841 **C** Place fields generated by the boundary vector cell model (Hartley et al., 2000). An
842 animal's perception of a trapezoidal environment (*right*) may be influenced by place-BVC
843 associations learned in a previous rectangular environment (*left*). In the trapezoid, simulated
844 place fields shift with the wall (**D**), causing similar distortion of the grid pattern.

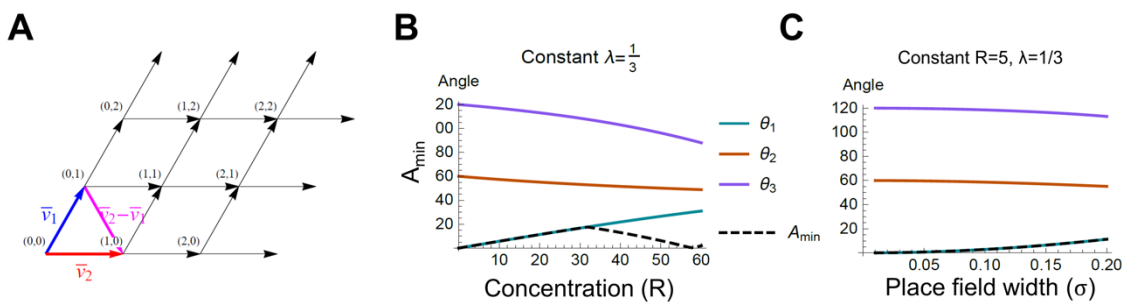


845

846 **Figure S3.** Grid distortions due to inhomogeneous environmental inputs in the *online* model.
847 **A)** When environmental inputs are concentrated in one corner of the environment (*top-*
848 *middle panel*), the resultant grid cell firing rate maps undergo a shearing distortion which
849 produces an orientation offset (A_{\min} ; *bottom-left panels*). This offset increases with
850 experience, as grid cell firing becomes increasingly dependent on the maturing sensory
851 inputs (*bottom-middle panel*), matching experiments in which rats always entered the box at
852 the same corner (*top-left panels*; Stensola et al., 2015). The size of the experimental and
853 simulated offsets are similar (*right panels*). **B)** Simulated distortions based on an exponential
854 decay in place cell input from one corner as a function of the decay parameter (R). **C)**
855 Concentrated place field input along one wall and both corners (*bottom left panel*) causes
856 another distortion pattern (*bottom right panel*) also observed experimentally (*top adapted*
857 from Stensola et al., 2015).



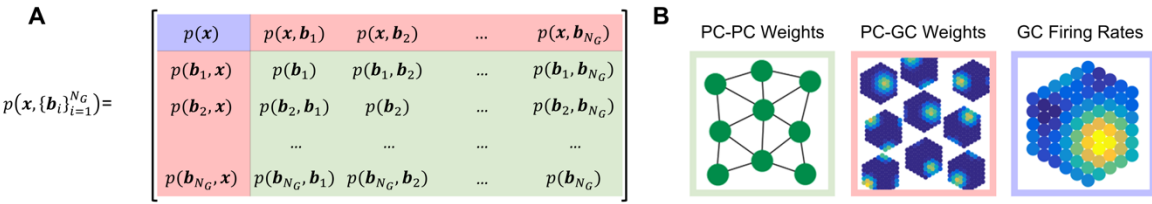
860 **Figure S4** Mathematical analysis of shearing of the grid pattern due to inhomogeneous
861 environmental inputs. **A** The orientation resulting from the shearing operation can be
862 calculated by analysing the angles of the sheared hexagonal lattice describing the centroids
863 of the grid fields. **B, C** The analysis predicts that the orientation offset should be dependent
864 on both the strength of the place fields' density / firing rate imbalance R (see Supplementary
865 Methods 1.7 and Fig. 2) (**B**) and their tuning widths (**C**).



866

867

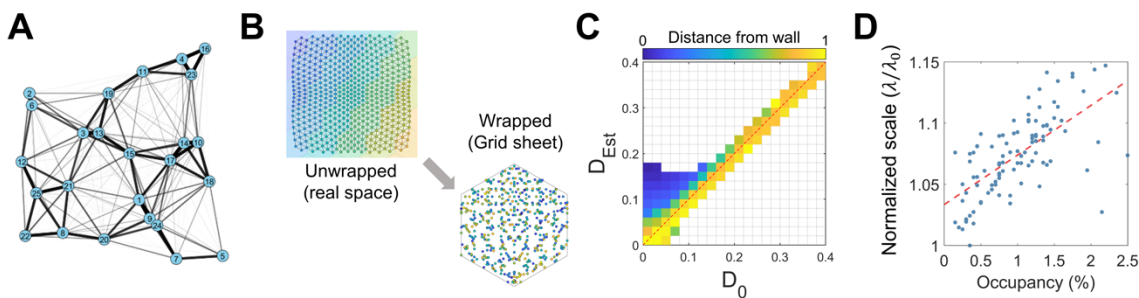
868 **Figure S5** Anatomy of a SLAM system. The joint location-map probability distribution (**A**) is
869 represented in the firing rates and synaptic weights within the HPB-mEC system (**B**).
870



871

872

873 **Figure S6 A** Spring network analogy of the associative structure of an environment. Edge
874 ‘stiffness’ is inversely proportional to the variance in the Gaussian observation. **B** ‘Wrapping’
875 physical space to encoded location on the grid sheet. Each colour indicates the tiling of the
876 based grid sheet’s domain in real space. **C** Pairwise distances near the edges of the
877 environment are overestimated due to under-sampling when the agent preferentially
878 explores the middle of an environment. Colours denote the distance of the pair of PCs i and
879 j from the walls of the $1 \times 1 \text{m}^2$ environment $d_{\text{wall}} = \sum_{p=i,j} \frac{1}{2} (\min(x_p, 1 - x_p) + \min(y_p, 1 -$
880 $y_p))$. **D** Resulting local scale is proportional to the occupancy. C When the grid scale is
881 smaller than the size of structure being encoded, we can think of ‘wrapping’ the structure
882 onto the grid sheet. Here, colours denoted different tilings of the base metric tile (the Voronoi
883 region of a given grid cell).



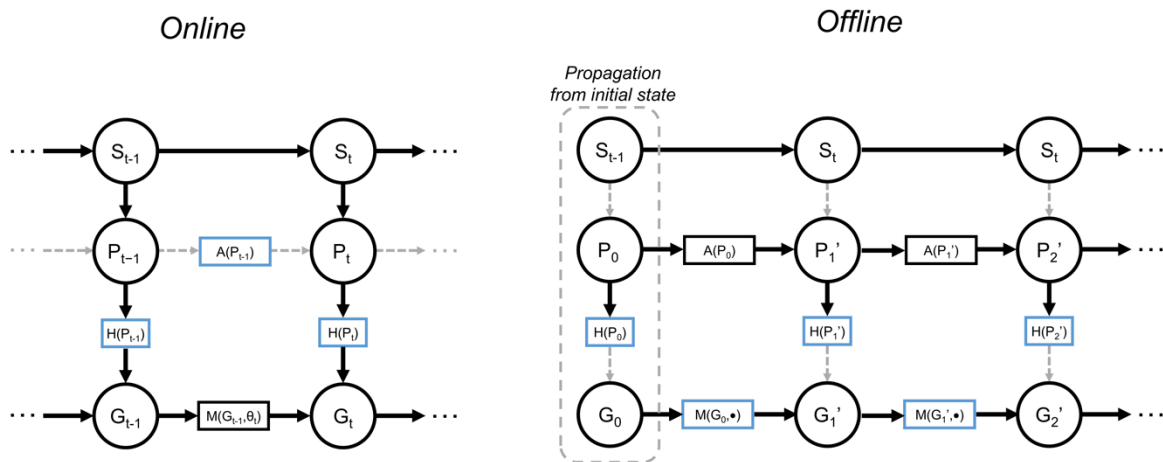
884

885

886

887

888 **Figure S7** An alternative view of the *online* and *offline* models. Place cells P are driven by
889 real-world stimulus S . During *online* exploration, the *associative* generative model is learned,
890 but does not generate predictions. During *offline* inference, the *metric* generative model is
891 corrected towards the predictions being generated by the *online* model, which becomes a
892 surrogate for sensory stimuli as would be generated by the real world model.



905

906

907

908

909 **Table S1** Algorithm detailing the overall dual-systems hypothesis of *online* and *offline*
910 localization and learning in the HPC/mEC.

Algorithm: <i>Online</i> localization and mapping with prediction error initiated <i>offline</i> inference	
1: initialize: $\mathbf{A} \sim \mathbb{U}(0, \Delta)$, $\mathbf{B} \sim \mathbb{U}(0, \Delta)$	% Initialize weights to small values $\sim \Delta$
2: while $k < K$ do:	% For the duration of the simulation
3: do_movement_update();	% Update state via path integration
4: make_observation();	% Compute PC firing
5: if $\epsilon_k > \epsilon_0$ do:	% If prediction error, do <i>offline</i> inference
6: while any $\tau_i < \tau_{min}$ do:	% Loop until cells below tension threshold
7: $u = \text{argmin}(\tau)$;	% Find node with max. message tension
8: compute_and_broadcast_message(u);	% Broadcast message to neighbours of u
9: for $t \in \text{Neighbours}(u)$ do:	% Loop over neighbours of u
10: update_belief(t);	% Update belief of node t
11: update_message_tensions(t);	% Compute change in belief of node t
12: update_PC_GC_weights();	% Do <i>associative</i> to <i>metric</i> map learning
13: update_PC_PC_weights();	% Update <i>associative</i> weights
14: do_measurement_update();	% Correct state estimate

911

912

913